A numerical performance analysis of a ducted, high-solidity tidal turbine in yawed flow conditions

Mitchell G. Borg[a], Qing Xiao[a,*], Steven Allsop[b], Atilla Incecik[a], Christophe Peyrard[c]

[a] *Department of Naval Architecture, Ocean, and Marine Engineering*
University of Strathclyde
Glasgow, Scotland, United Kingdom
[b] *Industrial Doctoral Centre for Offshore Renewable Energy (IDCORE)*
University of Edinburgh
Edinburgh, Scotland, United Kingdom
[c] *Electricité de France Research and Development*
EDF R&D
Chatou, Ile-de-France, France

Abstract

Analysing the fluid dynamic performance of a bare rotor when succumb to yawed flow conditions has consistently presented a diminishment in mechanical power conversion efficacy. Introducing a duct along the rotor perimeter has been acknowledged to sustain performance, yet the causation behind this phenomenon is uncertain. This study puts forward an investigation into the hydrodynamic performance concerning a true-scale, ducted, high-solidity tidal turbine in yawed free-stream flows by utilising blade-resolved, unsteady computational fluid dynamics. Investigating the performance within an angular bearing range of 0^o to 45^o with the turbine axis, increases in mechanical rotational power and thrust are acknowledged within a limited range at distinct tip-speed ratio values. Through the multiple yaw iterations, the maximum attainment falls at an angle of 23.2^o, resulting in a power increase of 3.44% to a peak power coefficient of 0.35 at a nominal tip-speed ratio of 2.00, together with an extension of power development along higher tip-speed ratios. In verification of the power increase, the outcomes are analysed by means of linear momentum theory; by utilising area-averaged values of static pressure acquired from annular radial surfaces fore and aft of the rotor, an analogous relationship with the blade-integrated outcomes is attained. The analysis concludes that, at higher tip-speed ratios, the pressure drop across the rotor increases at limited flow bearings, enhancing the resultant axial force loading upon the blades, hence providing further performance augmentation of the ducted, high-solidity tidal turbine.

Keywords: turbine performance, yawed flow, high solidity, open centre, tidal turbine, ducted tidal turbine, RSM

*Corresponding author
Email addresses: mitchell.borg@strath.ac.uk (Mitchell G. Borg), qing.xiao@strath.ac.uk (Qing Xiao)

1. Introduction

Efforts to improve upon the efficacy of energy-generating turbines have been in development following global market implementation. At the forefront of the pertinent research are efforts to increase mass-flow through the rotor, sustain power generation in yawed flow conditions, and augment wake flow to facilitate further turbine installations [1]. From the research attained, bi-directional ducts have been installed around a turbine rotor for performance enhancement as a result of the acceleration of axial flow velocity through the duct throat due to the induced Venturi effect and pressure discrepancy between the inlet and outlet. The system has been regarded to maintain axial flow velocity through the duct when succumb to yawed flow, thereby sustaining the performance of a rotor [2, 3, 4]. Yet, despite the potential improvements, the performance capacities of a bi-directional ducted rotor within yawed flow conditions are inadequately understood.

Few research ventures have tackled investigating the fluid dynamics of a duct-feature implementation in a turbine system within misaligned flow conditions [2, 3, 4, 5]. Establishing free-stream bearing variations ranging from $\pm\ 15^o$ to $\pm\ 60^o$, the analyses have concurred the enhancement of generated power as a result of a ducted rotor being succumb to a flow bearing, limited to a definitive yaw angle. Explicit evidence of the circumstances inducing the augmentation, however, has not been consistent. Igra [4] argued that the limited increase was directly associated with the lift produced by the aerofoil cross-section properties of the shroud. Phillips [5] claimed the improved performance was attributed to the slotted diffuser design, which injected pressurised flow from the free-stream for boundary-layer control along the diffuser interior. Albeit the advantageous results from the studies, the validity of the outcomes have been disputed due to uncorrected blockage effects of the structures within the testing facilities. More recent investigations upon tidal turbine systems similarly presented power augmentation, yet forms of methodological limitations had been portrayed, such as discretising the blade structure into elements [6, 7], rather than portraying its true physicality, or undefining the physical effects behind the resultant variation in rotor performance [8].

Evidence of rotor performance enhancement when installed within a shroud has been proclaimed within several decades of research disseminated from pioneering analytical [9] and experimental [2] investigations. The thrust and power generated are enhanced due to the increased dynamic loading upon the rotor as a result of the pressure drop augmentation through the duct. In defining the efficiency of the structure, analytical investigations have indicated that the power enhancement is instigated dependent on the diffuser arrangement and configuration. Cylindrical bi-directional ducts have been established to exhibit no performance improvements once the duct exit area is considered [9]. The flow along the turbine frontal area is directed through the rotor at the throat as a result of the low-pressure region developed immediately downstream. The power per rotor area is increased by a factor equivalent to the duct-to-rotor area ratio. In contrast, ducted turbines with a non-unity inlet to outlet area ratio, hence uni-directional, have been deduced to establish a peak power coefficient of 1.96, equivalent to a 3.3 augmentation factor magnitude higher than the Betz limit [10]. This is attained due to the degree of flow drawn in from a greater area upstream

than that interacted by a similarly-sized rotor in open flow.

Attributable to the potential augmentation in power extraction as a result of the increase in mass-flow, several commercial endeavours had adopted ducted turbine technology to achieve economic prospects. Amongst the ventures, DCNS/OpenHydro Ltd. had designed an open-centre ducted design approach [11, 12]. In open-water trials, a 2 MW turbine was successfully installed in the Bay of Fundy, Canada, together with a pair of 500 kW rated capacity turbines, as a demonstration array in Paimpol-Bréhat, Northern France, in collaboration with EDF France.

Experimental investigations have established the variation in mass-flow and fluid-structure interaction parameters by means of vacant, disc-embedded, and rotor-embedded shrouds. The analyses acknowledged the axial velocity and static pressure drop enhancement through the duct [2, 13]. Further performance enhancement was attained by means of minor components, notably flapped ring wings and boundary layer control auxiliary slots [14, 15, 16], in accompaniment to a diffuser within aligned and yawed flows. In acknowledging the effect of yawed flow upon the duct, an increase in power generated has been established at distinct angles, with performance sustainment at up to $\pm 30^o$ [17, 18]. The outcome was present equivalently present at both positive and negative bearings in relation to the variation of resultant angle-of-attack at the rotor blades [8, 19]. These outcomes distinguish from bare rotor analyses at yawed flow, which have depicted a diminishment in power output [20].

Numerical analyses have replicated experimentation, yet instated a multitude of parametric variations, together with more holistic data acquisition, due to ease of domain manipulation. Implementing a momentum sink within a computational fluid dynamic model has mirrored actuator disc theory and disc-embedded experimentation [21, 22, 23]. Similar drawbacks have, however, been brought about with the absence of radial load distribution and swirl in the rotor wake. Successful validation to experimentation [24] and evidence of performance enhancement, moreover at yaw angled free-stream bearings [25], has been attained [26, 27]. In overcoming the detriments of area-averaged disc modelling, blade-element momentum theory has been coupled to the computational domain in analysing yawed flow, acknowledging an increase in resultant power [6, 28]. Furthermore, rotor-explicit analyses have been undertaken, yet have utilised a relative velocity formulation of the governing equations, predominantly implementing a segment of the turbine, rather than a transient rotational sequence [29, 30, 31, 32].

The potential rotor power enhancement at a free-stream flow bearing variation with the turbine axis, and its causation, is of particular interest. The performance of a vacant, bi-directional, open-ended, true-scale duct succumb to variable conditional parameters within yawed flow conditions has been analysed [33]. The outcomes presented a 4.08% increase in axial velocity through the duct throat. However, the implementation of a high-solidity rotor with an open-centre within the duct shall induce variant pressure and velocity gradients. The resultant performance of the ducted turbine, as a result of the fluid-structure interaction, is therefore uncertain.

The numerical analysis elaborated in this present study has put forward a continuation of Borg et al. [33, 34, 35]. Primarily, a real-scale computational fluid dynamic model was developed to assess the hydrodynamic performance of a high-solidity open-centre rotor within

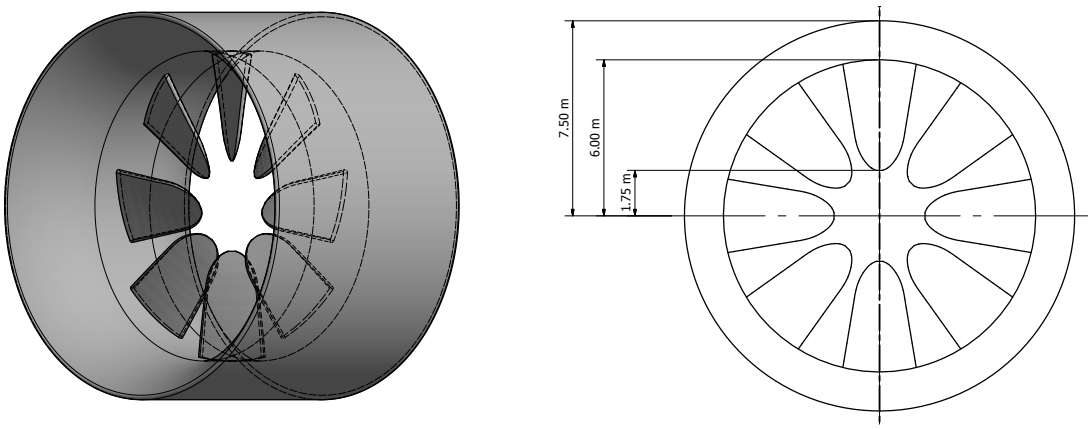

(a) Rendered three-dimensional CAD representation

(b) Cross-sectional projection

Figure 1: Geometrical model of the ducted tidal turbine [34]

a bi-directional duct in aligned flow conditions. Validation of the CFD model for tidal turbine applications was acquired [34]. Additionally, the numerical outcomes of the full-scale ducted turbine in aligned flow conditions were attained and compared to literature [36] and blade-element momentum theory [37].

In recognition of the variance in tidal stream direction at flood and ebb [38, 39], this investigation strived to overcome the related limitations by implementing a numerical analysis with blade-resolved actuality. The individual blades, rather than an area-averaged disc, were hence established. This permitted three-dimensional flow modelling of the turbine domain, together with induced turbulence effects. The aim of this research was to analyse the hydrodynamic performance of a ducted, high-solidity tidal turbine within yawed flow conditions, and pinpoint the causation of the performance augmentation. By means of this investigation, the variation in rotor performance at distinct bearings was acknowledged to establish the nominal flow-stream parameters. Area-averaged static pressure and axial velocity properties within the duct were acquired to verify and elaborate the outcomes by means of linear momentum theory.

2. Numerical Methodology

2.1. Physical Setup

As elaborated in Borg et al. [34], to attain a validated CFD model for tidal turbine applications, simulations were established to numerically replicate experimentation undertaken by Mycek et al. [40]. Identical blade, nacelle, and mast geometry were utilised within the model domain, illustrated in Figure 3, onto which a tetrahedral mesh was imprinted. The general dimensions of the turbine include a diameter D of 0.7 m, a nacelle length of 2.5 m, and a mast length of 1 m; supplementary descriptions may be attained within the literature. A distinction is present, however, between the physical aspects of the experimentation and

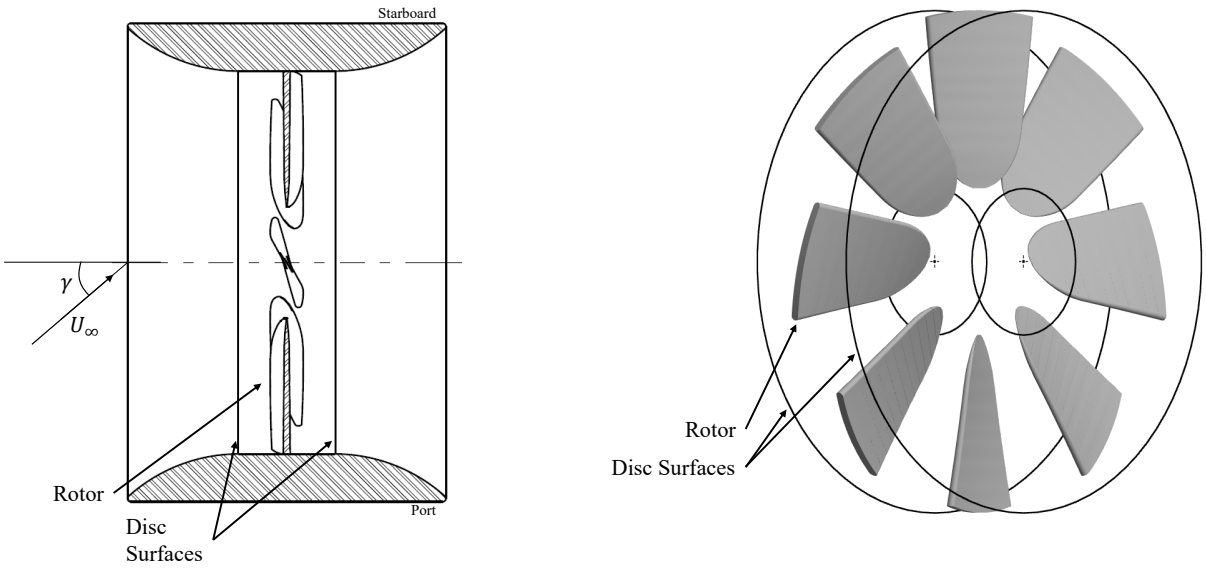

(a) Flow bearing orientation along turbine section

(b) Data acquisition planar annular surfaces in relation to rotor

Figure 2: Notation of incoming flow bearing in relation to rotor axis & positions of data acquisition planar annular surfaces

the numerical model. In the prior, the nacelle mast protrudes through the free-surface to connect to the above support, whereas, in the latter, only the submerged length of the mast is considered, with a hemisphere at the tip to avoid tip-induced vortices. Hence, a physical assumption is present within which the drag forces on the mast are solely considered to be due to the current, rather than any additional wave & wind factors. Albeit, due to the fact that waves were not induced in the experimentation, and that the setup was in a closed environment, the assumption that free-surface and topside effects were insignificant when considering the induced physics of the turbine was held. The parameters of the turbine and fluid flow were also instated from the literature, with a constant free-stream velocity of 0.8 m/s, a tip-speed ratio (TSR) range of 1.00 - 8.26, an inlet turbulent length scale of 1 m, and an inlet turbulence intensity of 3%.

In representation of the ducted high-solidity turbine, the model dimensions described a duct diameter (D) of 15 m, a rotor diameter (D_{rtr}) of 12 m, a hub diameter (D_{hub}) of 3.5 m, and a duct length (L_{dct}) of 10 m, as illustrated in Figure 1. The hydrofoil sections comprising the rotor blades consisted of a flat-plate design with rounded edges. The external hydrofoil geometry was quasi-identical to Allsop et al. [41], yet adapted to attain a more homogeneous blade surface. The geometry was provided by EDF R&D to replicate the outcomes of a turbine similar to the design of the OpenHydro PS2 device.

The domain parameters were instated from real-world data as reported in Neill et al. [42] and Bahaj and Myers [43], which described maximum acquired spring tide velocities of 4.0 $\mathrm{m.s^{-1}}$ and surface velocities of 5.0 $\mathrm{m.s^{-1}}$, respectively. In addition, Pham and Martin [38] and

Pham and Pinte [39] conducted numerical models to simulate the tidal cycle at the Paimpol-Bréhat site. An asymmetric velocity was acknowledged in both magnitude and direction, at ebb and flood, with an average-depth angular discrepancy of 20^o. For this reason, a free-stream velocity of 4.0 m.s^{-1} was implemented within a yaw bearing (γ) angular range of 0^o to 45^o. The bearing range was analysed in iterations of 15^o, in addition to a bearing of 23.2^o, which was equivalent to the geometrical gradient of the inlet rim, incoming from the turbine port direction, as illustrated in Figure 2a. An inlet turbulence intensity of 3% and an inlet turbulent length scale of 1 m were instated. Within this free-stream variation, a turbine tip-speed ratio (TSR) range of 1.00 - 2.50 was considered.

2.2. Computational Setup

Correspondent to Borg et al. [34], the numerical model was designed to be a fully submerged system within a constant fluid flow. Far-stream effects from the free-surface and seabed were therefore abdicated. This setup permitted the performance analysis of the ducted turbine under consistent temporal conditions. The commercial solver ANSYS Fluent 19.2 was utilised in computing the continuity and Navier–Stokes equations. An Unsteady Reynolds-averaged Navier–Stokes (URANS) turbulence model was implemented in mathematical closure to represent flow property fluctuation within the three-dimensional, unsteady, incompressible flow field.

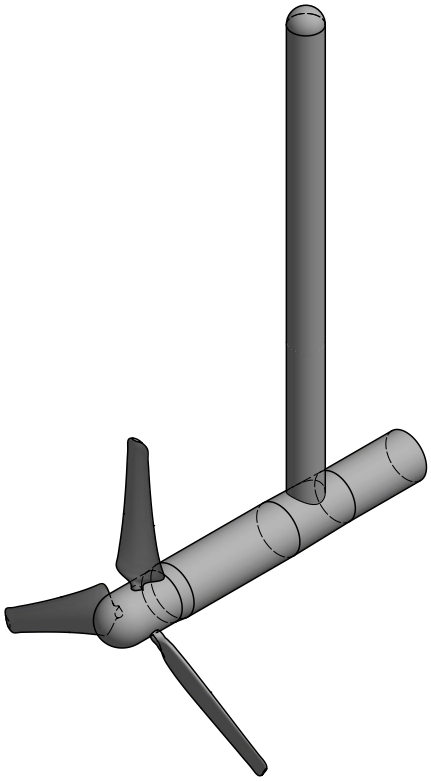

Figure 3: Rendered three-dimensional CAD representation of the horizontal-axis tidal turbine [40] utilised for the validation of the CFD model [34]

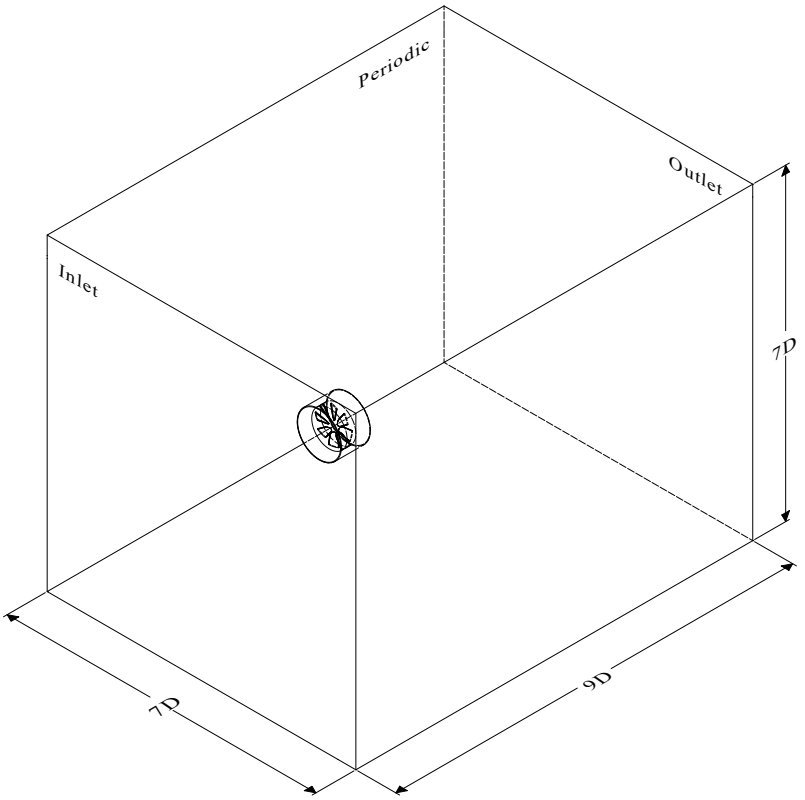

(a) Layout of the ducted turbine domain

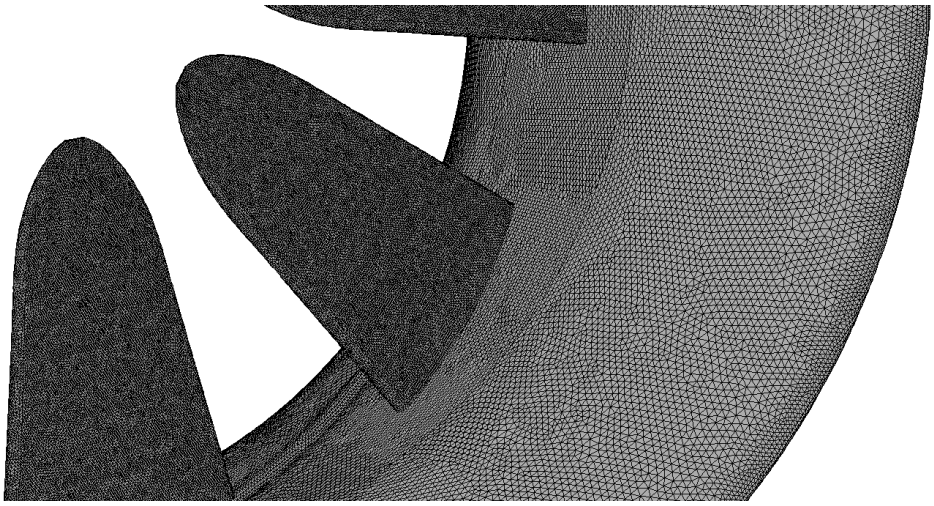

(b) Geometric tessellation of the mesh on the duct and rotor blades

Figure 4: Representation of the domain and turbine mesh [34]

Establishing a cuboidal domain layout, a cross-sectional quadratic-face edge-length of $7D$ was utilised. The ducted turbine was positioned at the centre of the vertical plane. The dimensions of the computational domain attained a numerical areal blockage ratio of

less than 2% to the external duct diameter to ascertain the absence of far-field effects [44]. A domain length of $9D$ was implemented, where the inlet and outlet planes were situated at a distance $3D$ upstream and $6D$ downstream of the duct, respectively, as illustrated in Figure 4. The dimensions of the domain were therefore equivalent to 105 m by 105 m by 135 m. The domain surrounding the turbine rotor was segregated from the global domain to induce a moving mesh model with rotation at the turbine rotor relative to a stationary outer domain, with interfaces between the two domains. The no-slip wall condition was implemented on the duct & rotor surfaces. Periodic conditions were allocated to the domain boundaries parallel to the turbine axis. Velocity inlet and pressure outlet conditions were allocated to the perpendicular boundaries. The velocity yaw angle (γ) was induced by varying the incident velocity components at the inlet boundary.

In addition, two pairs of planar numerical surfaces were introduced equidistant on either side of the rotor. The primary surface was a circular plane of diameter D_{rtr}. The secondary surface was an annular plane of inner and outer diameters D_{hub} and D_{rtr}, respectively. The prior represented the cross-section of the duct throat, whereas the latter represented the rotor profile with an open-centre. Both planes were introduced within the numerical model at a distance $0.125D_{rtr}$ fore and aft of the rotor, as illustrated in Figure 2b. These numerical surfaces were utilised for data acquisition purposes to attain area-averaged values of normalised axial velocity and static pressure within the turbine duct throat.

The Standard Reynolds Stress Model (RSM) 'Stress-Omega' (τ-ω) turbulence model was utilised with the SIMPLE pressure-velocity coupling scheme setting, the Green-Gauss node-based gradient, pressure staggering option (PRESTO) pressure, second order upwind momentum, second order upwind specific dissipation rate, and second order upwind Reynolds stresses spatial discretisation settings, and the bounded second order implicit transient formulation setting were utilised as the solution methodologies. The Reynolds–Stress Model was preferred to close the Navier-Stokes equation as the Reynolds stresses are solved in three-dimensional space due to the non-implementation of the Boussinesq assumption, prompting superiority in analysing anisotropic flows, such as flows over curved surfaces, flows in rotating fluids, and flows in ducts with secondary (rotational) motion [45]. In addition, the effects of streamline curvature, swirl, rotation, and rapid changes in strain rate are considered in a more effective manner than one-equation or two-equation models. The time-step considered was designated in relation to the tip-speed ratio of the rotor, where each transient iteration was temporally equivalent to one-half of a degree of a turbine revolution, therefore attained by:

$$\Delta t_{step} = \frac{\pi}{360 \cdot \Omega_{sys}} \tag{1}$$

where Δt_{step} is the time-step and Ω_{sys} is the turbine rotational velocity. The described numerical setup had been validated in previous works. The validation procedure consisted of a numerical-experimentation comparison of a small-scale tidal turbine. Details in relation to the setup of the numerical validation model may be attained in Ref. [34].

A tetrahedral mesh was imprinted upon the turbine domain geometrical model. A mesh independence procedure, described in Table 1, was carried out on the ducted turbine by considering the parameter with the highest degree of dynamics. The mesh independent

parameters for the fluid-structure interaction were established utilising ITTC recommended meshing procedures and guidelines [46]:

$$\varepsilon_n = S_n - S_{n-1} \tag{2}$$

$$\Psi = \frac{\varepsilon_n}{\varepsilon_{n-1}} \tag{3}$$

where Ψ is the convergence ratio, ε is the difference between the considered variable (S) at different mesh independence study iterations, and the subscript n is the mesh independence study iteration. The turbine torque coefficient (C_Q) was utilised as the mesh independence considered variable (S).

Table 1: Mesh independence analysis for the ducted, high-solidity tidal turbine

n	Cell Number	Cell Number Ratio	S	ε	Ψ
3	$18,621,356$	1.440	0.1121	-0.00890	0.4113
2	$12,932,325$	1.270	0.1032	-0.02164	
1	$10,185,673$		0.08156		

Subsequent to the procedure, the final average surface mesh count utilised was marginally above 94,000 cell faces per blade, illustrated in Figure 4b, with more than 18.5 million volumetric cells within the entire domain, over 10 million of which within the turbine rotating region. The mesh was implemented with a prism layer at non-slip surfaces with an appropriate cell height to achieve a y-plus value of $60 \leqslant y^+ \leqslant 400$ across the blades and duct. This range was considered due to the high Reynolds number ($> 10^6$) of the system, hence modelling the viscous sublayer was abdicated to reduce computation time.

The CFD computations were performed using the ARCHIE-WeSt cluster facility at the University of Strathclyde by running two Intel Xeon Gold 6138 2.00 GHz computational nodes, with 40 cores and up to 192 GB of RAM per simulation. A ducted turbine simulation was completed within $\approx$ 110.5 wall-clock hours, equivalent to $\approx 4,420$ core-hours, hence resulting in an average of $\approx$ 5.5 wall-clock hours per turbine rotation.

3. Numerical Characterisation

3.1. Physical Modelling

In consideration of the analysis of a physical turbine, notable definitions concerning the resultant performance outcomes, in terms of the boundary conditions employed, are identified.

Utilised to attain open-ocean conditions, the blockage ratio (α_{bl}) is defined as a correlation between the device reference area (A_{dvc}) and the domain sectional area (A_{dmn}):

$$\alpha_{bl} = \frac{A_{dvc}}{A_{dmn}} = \frac{\pi R_{dvc}^2}{L_{dmn}^2} \tag{4}$$

where R_{dvc} is the device radius, and L_{dmn} is the length of the quadratic cross-sectional area of the computational domain.

The tip-speed ratio (TSR) is established as a correlation between the linear blade-tip velocity and the free-stream velocity:

$$TSR = \frac{|\Omega_{sys}|R_{rtr}}{U_\infty} = \frac{|\Omega_z|R_{rtr}}{U_\infty} \tag{5}$$

where Ω_{sys} is the system rotational speed, hence Ω_z is the axial angular velocity, U_∞ is the free-stream velocity, and R_{rtr} is the rotor radius.

To determine the turbine capacity in converting the fluid free-stream energy into rotational energy, the power coefficient (C_P) was established. This considered the mechanical rotational power attained by the device (P_{dvc}) as a ratio of the maximum rotational power potentially acquired in the device area (P_∞):

$$C_P = \frac{P_{dvc}}{P_\infty} = \frac{M_z\Omega_z}{\frac{1}{2}\rho A_{dvc}U_\infty^3} = \frac{M_z\Omega_z}{\frac{1}{2}\rho\pi R_{dvc}^2U_\infty^3} \tag{6}$$

where R_{dvc} is the device radius, M_z is the rotor torque.

In relation to the power generated, the torque coefficient (C_Q) evaluated the mechanical torque attained by the device (Q_{dvc}) as a ratio of the maximum torque potentially acquired in the device area (Q_∞):

$$C_Q = \frac{Q_{dvc}}{Q_\infty} = \frac{M_z}{\frac{1}{2}\rho A_{dvc}R_{rtr}U_\infty^2} = \frac{M_z}{\frac{1}{2}\rho\pi R_{dvc}^2R_{rtr}U_\infty^2} \tag{7}$$

In continuation, the resultant thrust on the device induced in a direction parallel to the turbine axis contributed to the fluid-structure phenomenon. The thrust coefficient (C_T) was quantified as a function of the device thrust (T_{dvc}) and the maximum thrust potentially induced upon the device area (T_∞):

$$C_T = \frac{T_{dvc}}{T_\infty} = \frac{F_z}{\frac{1}{2}\rho A_{dvc}U_\infty^2} = \frac{F_z}{\frac{1}{2}\rho\pi R_{dvc}^2U_\infty^2} \tag{8}$$

where F_z is the axial force induced upon the turbine.

In addition, as a flow bearing was introduced, the resultant force induced in a direction perpendicular to the turbine axis was present. The sway-force coefficient ($C_{F,x}$) was established as a function of the sway force induced perpendicular to the turbine axis (F_x), and the maximum force potentially induced (F_∞) upon the lateral area of the turbine:

$$C_{F,x} = \frac{F_x}{F_\infty} = \frac{F_x}{\frac{1}{2}\rho A_{dct}U_\infty^2} = \frac{F_x}{\frac{1}{2}\rho L_{dct}D_{dct}U_\infty^2} \tag{9}$$

10

To establish the flux through the rotor, the volumetric flow-rate coefficient ($C_{\dot{V}}$) evaluated the volumetric flow-rate of the fluid through the rotor ($\dot{V}_{rtr}$) as a ratio of the maximum volumetric flow-rate potentially attained within the duct:

$$C_{\dot{V}} = \frac{\dot{V}_{rtr}}{\rho A_{rtr} U_\infty} = \frac{\dot{V}_{rtr}}{\rho \pi R_{rtr}^2 U_\infty} = \frac{\rho \pi R_{rtr}^2 U_{res}}{\rho \pi R_{rtr}^2 U_\infty} = \frac{U_{res}}{U_\infty} \tag{10}$$

where U_{res} is the resultant velocity.

Furthermore, the induced axial velocity through the duct (U_z) was compared to the free-stream to attain a quantitative measure of the capacity of flow alignment to the turbine axis by means of an axial velocity coefficient ($C_{U,z}$):

$$C_{U,z} = \frac{U_z}{|U_\infty|} \tag{11}$$

Identically, the static pressure (P_s) was compared to the dynamic pressure of the free-stream to attain a static pressure coefficient ($C_{P,s}$):

$$C_{P,s} = \frac{P_s}{\frac{1}{2}\rho U_\infty^2} \tag{12}$$

Instituting linear momentum theory, the annular data-extraction planes were utilised to establish the coefficient of disc-thrust ($C_{T_{AD}}$) by acknowledging the difference between the pressure upstream (P_{s-up}) and pressure downstream (P_{s-dwn}) of the rotor:

$$C_{T_{AD}} = \frac{P_{s-up} - P_{s-dwn}}{\frac{1}{2}\rho U_\infty^2} \cdot \frac{A_{disc}}{A_{dvc}} = \Delta C_{P,s} \cdot \frac{A_{disc}}{A_{dvc}} \tag{13}$$

where A_{disc} is the planar disc area.

3.2. Computational Modelling

3.2.1. Conservation Modelling

The conservation of mass and momentum formulae were implemented within the CFD model in solving the flow domain:

$$\frac{\partial U_i}{\partial x_i} = 0 \tag{14}$$

$$\rho \frac{\partial U_i}{\partial t} + \rho U_j \frac{\partial U_i}{\partial x_j} = -\frac{\partial P_s}{\partial x_i} + \frac{\partial}{\partial x_j}\left(\mu\left(\frac{\partial U_i}{\partial x_j} + \frac{\partial U_j}{\partial x_i}\right) - \rho\overline{u_j' u_i'}\right) \tag{15}$$

where U_i is the Reynolds-averaged velocity, x_i is the Cartesian coordinate, t is the elapsed time, P_s is the fluid static pressure, μ is the fluid dynamic viscosity, and $-\rho\overline{u_j' u_i'} = \rho\tau_{ij}$ is the Reynolds-stress tensor.

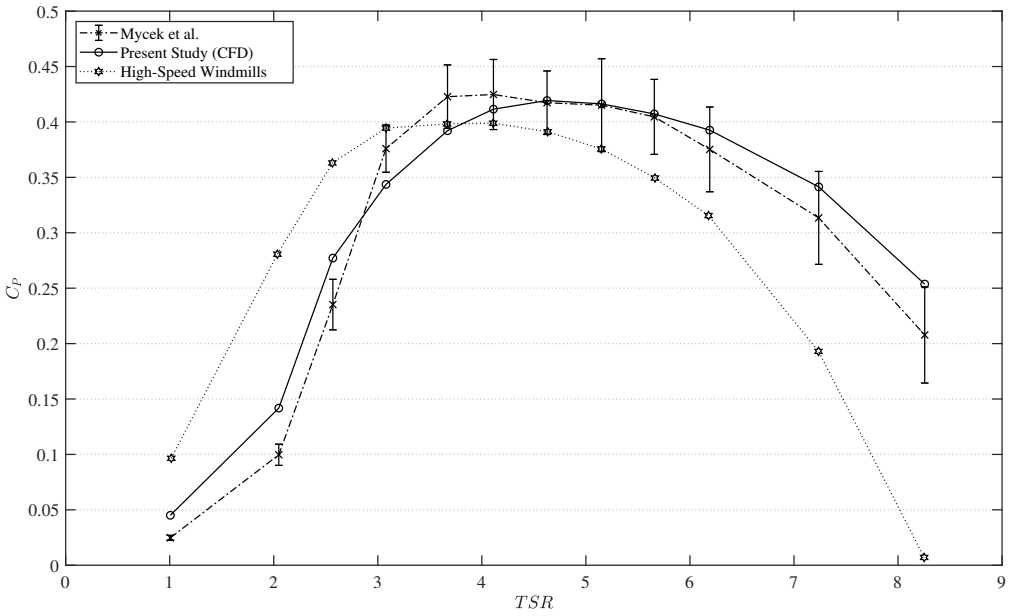

Figure 5: Power coefficient (C_P) in relation to tip–speed ratio (TSR) in validation of the CFD model [34]

3.2.2. Turbulence Modelling

To close the momentum conservation equation, the (τ-ω) turbulence model was implemented:

$$\rho\frac{\partial \tau_{ij}}{\partial t} + \rho U_k \frac{\partial \tau_{ij}}{\partial x_k} = \frac{\partial}{\partial x_k}\left[\left(\mu + \frac{\mu_T}{\sigma_k}\right)\frac{\partial \tau_{ij}}{\partial x_k}\right] - \rho P_{ij} - \rho \Pi_{ij} + \frac{2}{3}\beta^* \rho\omega k \delta_{ij} - 2\rho\omega_k(\tau_{jm}\epsilon_{ikm} + \tau_{im}\epsilon_{jkm}) \tag{16}$$

$$\rho\frac{\partial \omega}{\partial t} + \rho U_j \frac{\partial \omega}{\partial x_j} = \frac{\partial}{\partial x_j}\left[\left(\mu + \frac{\mu_T}{\sigma_k}\right)\frac{\partial \omega}{\partial x_j}\right] + \alpha\frac{\rho\omega}{k}\tau_{ij}\frac{\partial U_i}{\partial x_j} - \beta_o f_\beta \rho\omega^2 \tag{17}$$

where τ_{ij} is the specific Reynolds-stress tensor, k is the turbulence kinetic energy, ω is the specific dissipation rate, Π_{ij} is the pressure-strain correlation tensor, μ_T is the eddy viscosity, ω_k is the rotation vector, ϵ_{ijk} is the Levi-Civita pseudotensor, f_β is the mean rotation tensor factor, and α, σ_k, β_o, and β^* are closure coefficients.

4. Numerical Model Validation

Validation of the CFD model was attained in Borg et al. [34], where the power, torque, and thrust coefficients of a numerical tidal turbine were compared to experimentation performed by Mycek et al. [40] and high-speed windmill data by Betz [36]. The CFD model attained a coefficient of determination (R^2) of 0.955, 0.889, and 0.946 with the experimentation data points along the curves, respectively. Additionally, the numerical wake velocity profiles at distinct locations along the turbine wake were compared to the experimentation

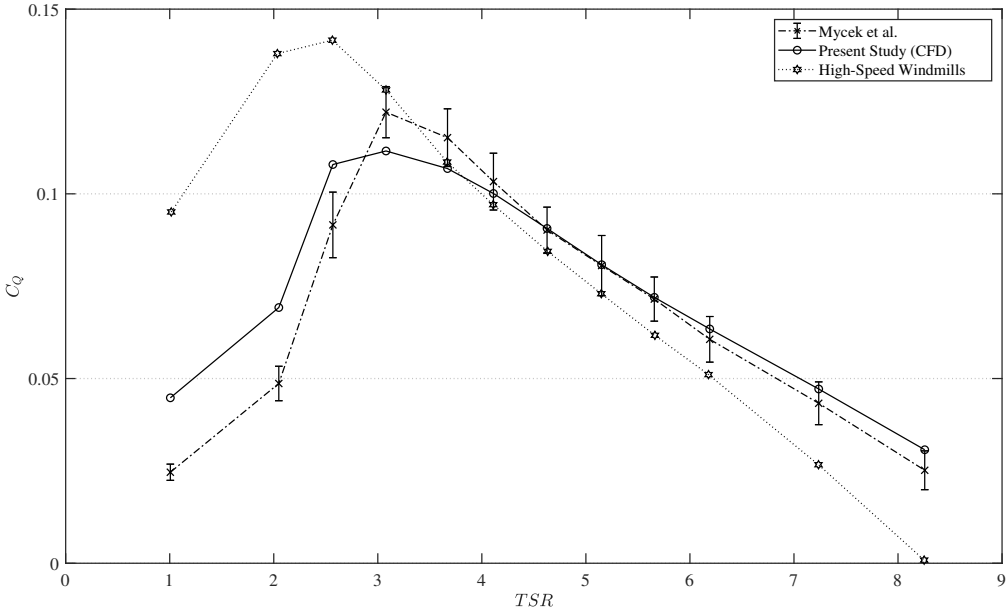

Figure 6: Torque coefficient (C_Q) in relation to tip–speed ratio (TSR) in validation of the CFD model [34]

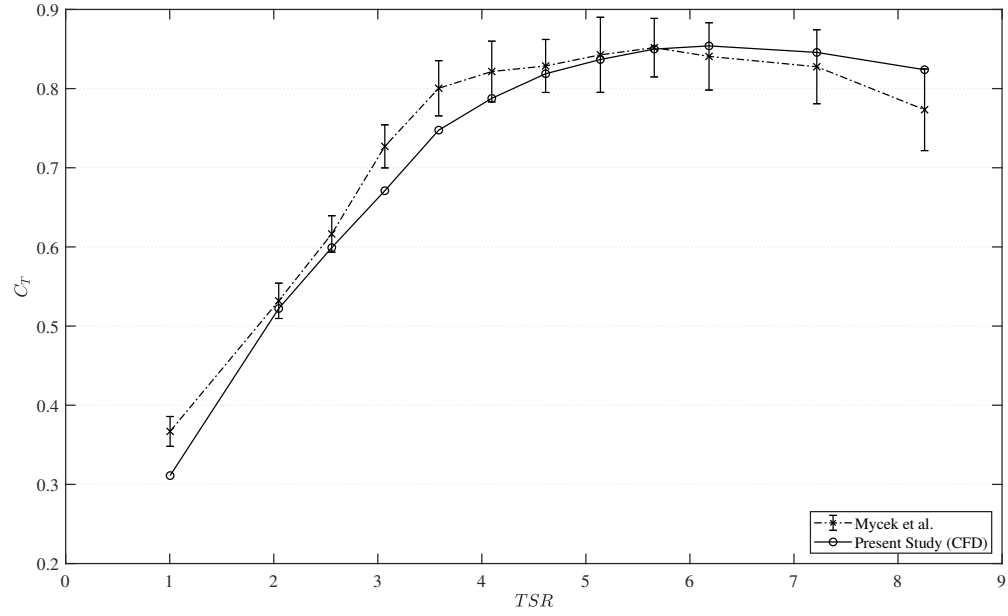

Figure 7: Thrust coefficient (C_T) in relation to tip–speed ratio (TSR) in validation of the CFD model [34]

data by Mycek et al. [40]. The power, torque, and thrust coefficient curves are illustrated in Figures 5, 6, and 7, respectively. The wake velocity profiles are illustrated in Figure 8.

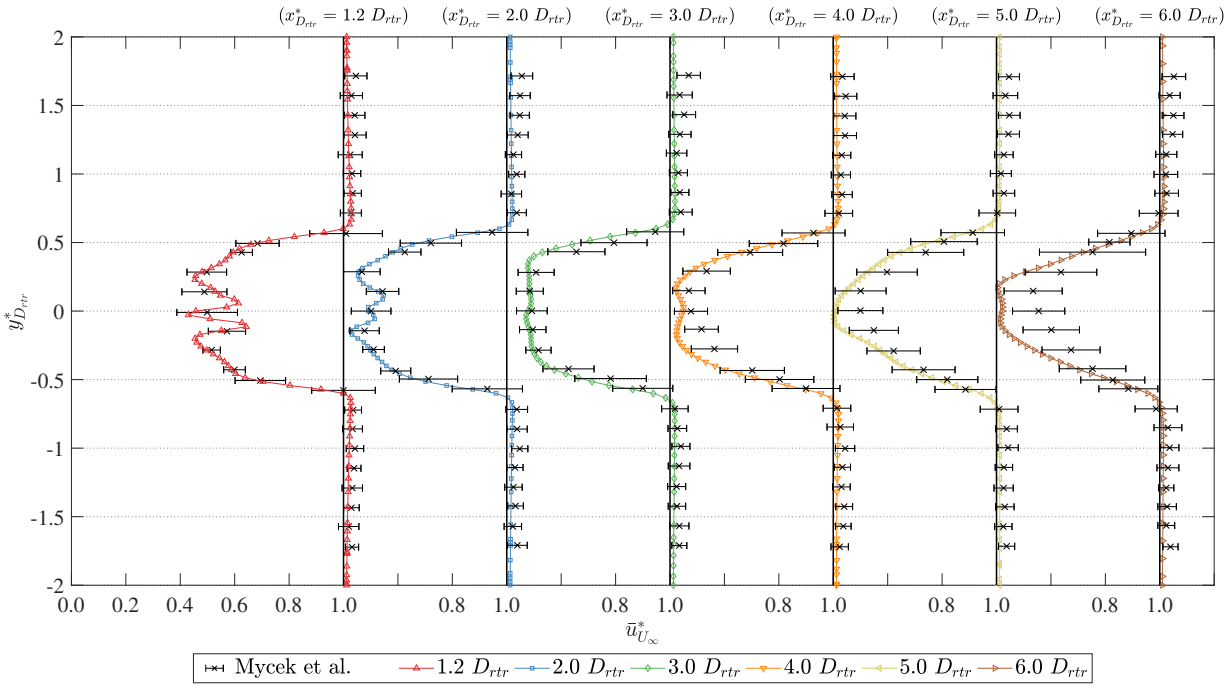

Figure 8: Comparative evaluation of the current horizontal-axis tidal turbine CFD model with experimentation [40] for the wake velocity profiles at distinct downstream displacements ($x^*_{D_{rtr}}$) at TSR 3.67 [34]

5. Performance of the Ducted High-Solidity Tidal Turbine in Yawed Flow

5.1. Power & Torque Coefficients

Prior investigations [34] of the ducted, high-solidity tidal turbine in aligned flow ($\gamma = 0^o$) had described a quasi-linear torque coefficient curve attaining a peak value of 0.292 at a TSR of 1.00, decreasing to 0.115 at a TSR of 2.50. Within yawed flow conditions, variations in the outcomes were evident along the TSR range, as illustrated in Figure 9. The quasi-linear correlation was sustained at the distinct bearings, yet the resultant torque increased at yaw angles of 15^o - 30^o and decreased at 45^o. On average, the induced torque varied by 2.52%, 4.52%, 2.35%, and -3.50% at bearings of 15^o, 23.2^o, 30^o, and 45^o, respectively. The statistical deviation of the torque data is illustrated in Figure B.27.

The augmentation in torque occurred due to the induced flow within the bi-directional duct in yawed flow conditions. Prior investigations [33] had numerically investigated the swallowing capacity of the vacant duct at identical bearings. The normalised axial velocity varied in relation to yaw bearing. The swallowing capacity of the duct was found to increase within a bearing range of 15^o - 30^o from aligned flow, with a decrease at a bearing of 45^o. This outcome transpired as a result of the variant static pressure within the duct throat. As linear momentum theory states that the torque generated by a rotor is proportional to the flow velocity through the rotor, the elaborated torque augmentation was therefore induced by the resultant flow acceleration through the duct.

In continuation, the power coefficient curve of the ducted, high-solidity tidal turbine in aligned flows ($\gamma = 0^o$) described a short spanning power coefficient curve attaining a peak

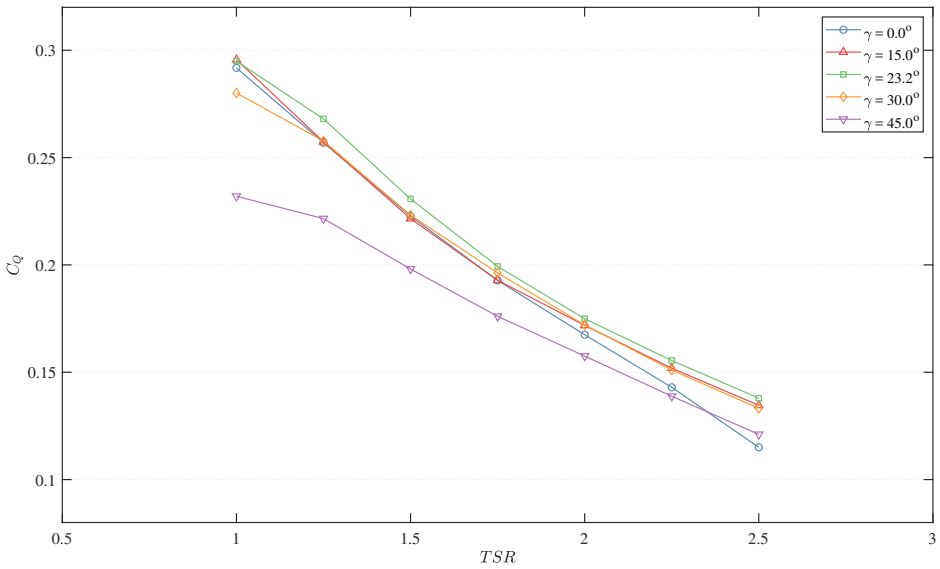

Figure 9: Evaluation of the mean ducted turbine torque coefficient (C_Q) at distinct flow bearings in relation to TSR

power coefficient of 0.338 at a nominal TSR of 1.75 within a range of 1.00 – 2.50. Within yawed flow conditions, the resultant power coefficient varied in relation to the induced torque. Illustrated in Figure 10, a notable outcome was the increase in peak power coefficient at the distinct bearings, surpassing that at aligned flow. Maximum increases of 1.90%, 3.86%, and 1.90% to values of 0.344, 0.350, and 0.344, at bearings of 15.0^o, 23.2^o, and 30.0^o, respectively, were defined. Diminished power was acknowledged at $\gamma = 45.0^o$; the decrease in power transpired as a result of a re-circulation zone generated upstream of the rotor. Further elaborated in Borg et al. [33] and Section 5.6 within this work, the re-circulation zone was induced due to the duct angle-of-attack with the free-stream. At the angle-of-attack, the low-pressure zone reduced the static pressure on the rotor upstream blade area, resulting in lower power & torque generated. As a result, the 23.2^o bearing was established to be the highest power generating condition.

Due to the augmentation in power coefficient, the variation in true power at the distinct yaw bearings was investigated, illustrated in Figure 11. From a null bearing, as the flow angle increased to 15^o, the power coefficient variation was the most substantial at higher TSRs (2.00 – 2.50). The 23.2^o bearing attained the highest performance values, establishing a power augmentation along the entire TSR range, with a peak mechanical power value of 1.975 MW. Subsequent bearings pertained diminishing performance values.

Further to the mean power generated, the transient output of the rotor was considered. The variation in power output with azimuth angle (ϕ_r) at the nominal tip-speed ratio of each free-stream bearing was investigated within five rotational cycles, as illustrated in Figure 12. When succumb to aligned flow, a variance in mechanical power was recognised due to flow fluctuations [34] as a result of vortex ring shedding. Within a bearing range of 15^o – 30^o, a diminishment in fluctuation was observed, signifing a reduction in vortex shedding effects.

15

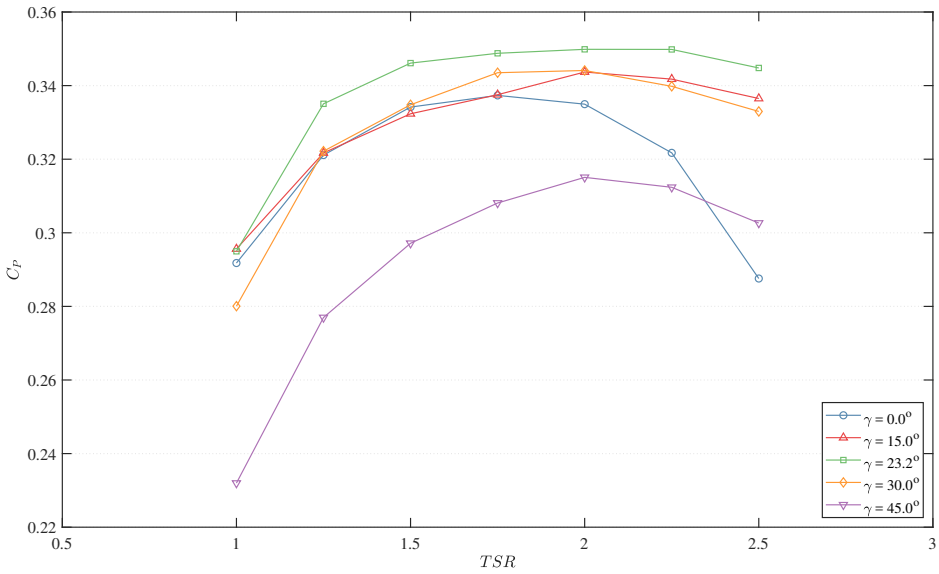

Figure 10: Evaluation of the mean ducted turbine power coefficient (C_P) at distinct flow bearings in relation to TSR

At a bearing of 45^o, synchronised outcome fluctuations were evident, with eight fluctuations per cycle, equivalent to the rotor blade number. The fluctuations were acknowledged to be due to the low pressure induced by the re-circulation zone.

Due to the fluctuations within a rotation cycle, the mean response of a rotor blade during its rotation, illustrated in Figure 13, was analysed. The outcome throughout the rotation was attained by synchronising the output of each of the eight blades along five cycles by azimuth angle, and subsequently averaging the output per blade per cycle at each azimuth angle. A cycle-averaged disc output was thereby attained. The output was multiplied by the blade number for comparison purposes.

At aligned flow ($\gamma = 0^o$), the mean performance was consistent along the turbine rotation. Upon the introduction in flow bearing ($\gamma = 15^o, 23.2^o, 30^o$), the free-stream velocity induced perpendicular and parallel vector components to the rotor plane. Due to the local flow acceleration along the cross-sectional plane parallel to the rotor axis [33], the angle-of-attack augmented, skewing the resultant performance.

In a cylindrical coordinate system, at $\phi_r = 90^o$ and $\phi_r = 270^o$, the rotational velocity vector of the rotor blade foil acted along the tangential axis, whereas the free-stream vector components acted along the axial and radial axes. Therefore, as the local flow accelerated, a variation in the angle-of-attack along the blade was induced, resulting in a power generation increase in comparison to that within aligned flow.

At azimuth positions $\phi_r = 0^o$ and $\phi_r = 180^o$, the rotational velocity vector of the rotor blade foil acted along the tangential axis, with the free-stream vector components acting along the axial and tangential axes. As the rotational velocity vector was present in opposite directions on a two-dimensional plane at the two positions, the interaction of the tangential vectors diminished and enhanced the angle-of-attack, at $\phi_r = 0^o$ and $\phi_r = 180^o$ respectively,

16

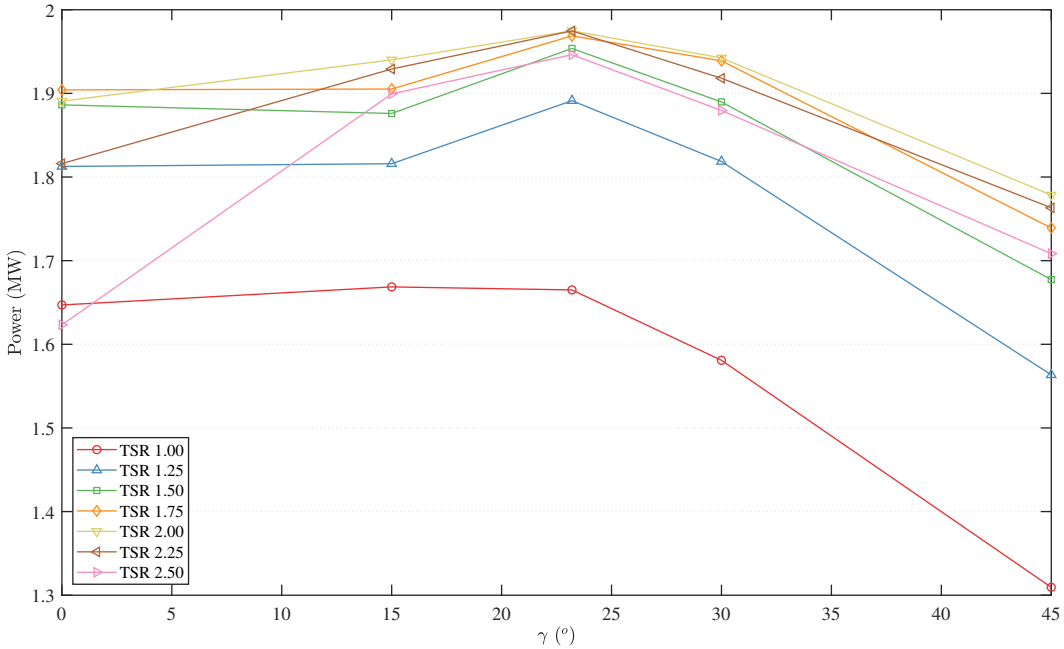

Figure 11: Evaluation of the true mean power at nominal TSR in relation to flow bearing (γ)

resulting in the variation in power generation. The free-stream bearing of $\gamma = 45^o$ brought about a notable outcome, with a significant dip in efficiency at $\phi_r = 90^o$.

5.2. Thrust Coefficient

In recognition of the torque enhancement within a distinct flow bearing range, it was evident that the loading upon the blades had increased. To ascertain this aspect, the thrust coefficient of the system, together with duct and rotor discretisation, was investigated.

Within aligned flows, the turbine system curve portrayed a peak value of 1.08 at low TSR, which decreased in a polynomial manner to 0.77 at high TSR. When succumb to yawed flows, a coefficient increase was acknowledged at bearings of 15^o and 23.2^o, distinctively at higher TSRs, as illustrated in Figure 14. The highest values of thrust throughout the TSR range were attained at the 23.2^o bearing, with a thrust coefficient of 1.10 at low TSR, decreasing to 0.91 at high TSR. The rotor was succumb to $\approx 69\%$ of the total axial load. The system thrust diminished at 30^o and 45^o flow bearing. The statistical deviation of the thrust data is detailed in Figure B.28.

Solely acknowledging the rotor thrust, the variation with TSR resembled that of the torque coefficient, which defined a quasi-equivalent outcome as $\gamma = 0^o$ at $\gamma = 15^o, 30^0$ with an increase at higher TSRs. An enhancement in thrust was established at $\gamma = 23.2^o$, with a diminishment at $\gamma = 45^o$. Due to the increase in thrust and torque at higher TSRs, it was therefore evident that a higher degree of axial force loading was induced within the flow parameters.

17

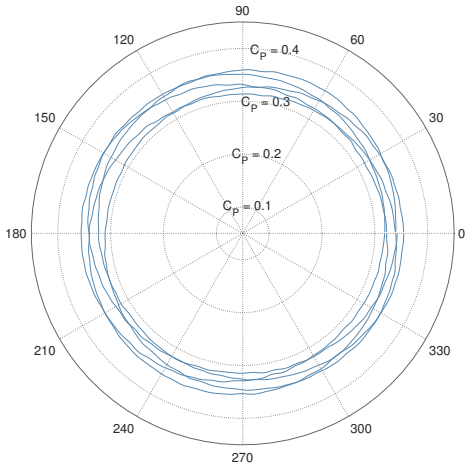

(a) $\gamma = 0.0^o$

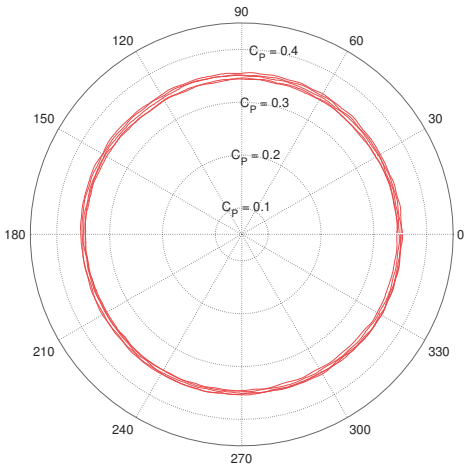

(b) $\gamma = 15.0^o$

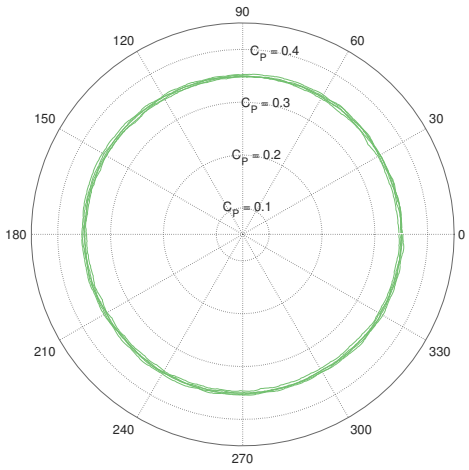

(c) $\gamma = 23.2^o$

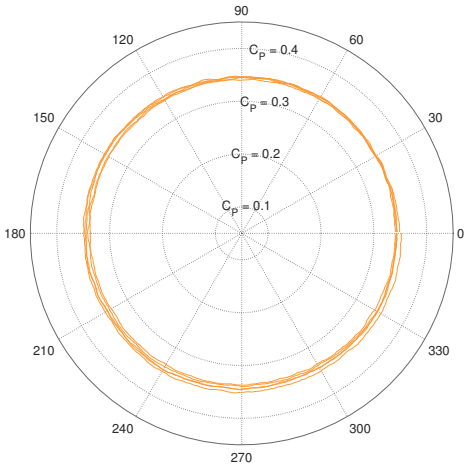

(d) $\gamma = 30.0^o$

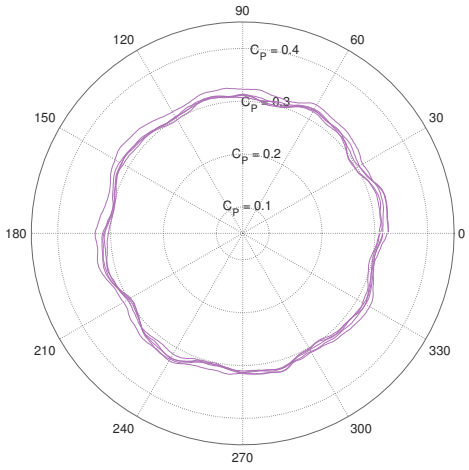

(e) $\gamma = 45.0^o$

Figure 12: Instantaneous ducted turbine power coefficient (C_P) along rotary operation in relation to blade azimuth angle (ϕ_r) at nominal TSR

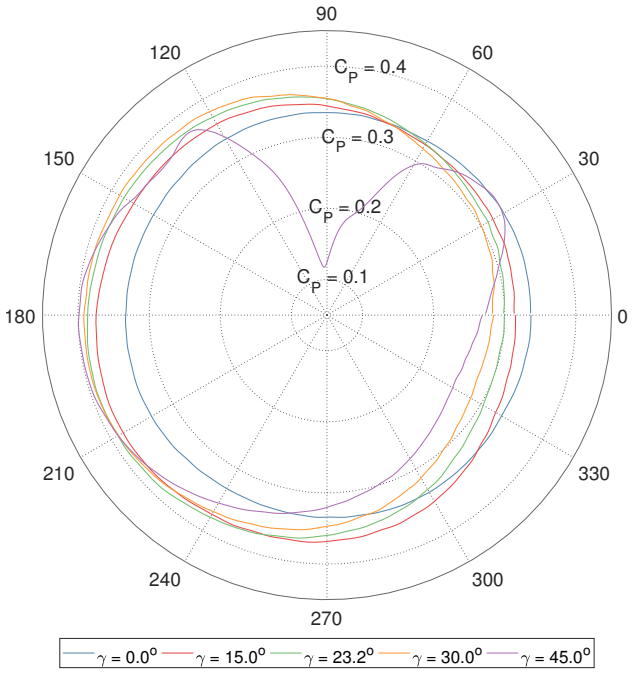

Figure 13: Evaluation of the mean single-blade response (C_P) in relation to azimuth angle (ϕ_r) at a TSR of 1.75

5.3. Linear Momentum Analysis

5.3.1. Axial Velocity Coefficient & Volumetric Flow Rate Coefficient

Utilising the data-acquisition planar surfaces introduced fore and aft of the rotor, the area-averaged axial velocity was analysed as equivalence at both planes was acknowledged. Illustrated in Figure 15, the axial velocity through the duct was consistent along the yaw bearing range, specifically at high TSR values, acting in proportion to the turbine rotational velocity. The highest axial flow values were attained at the nominal bearing of $\gamma = 23.2^o$. Within the analysis, a maximum coefficient of 0.84 was achieved at high TSR. This outcome portrayed the capacity of the shroud installation in sustaining axial velocity through a rotor when succumb to yawed free-stream velocities.

Furthermore, the volumetric flow rate was detailed, illustrated in Figure A.26. This was established to acknowledge the true flow through the duct, as the axial velocity through the duct solely represented the axial component of the resultant flow vector, moreover at high free-stream bearings. The axial velocity coefficient was $\approx 98\%$ of the volumetric flow rate coefficient.

5.3.2. Static Pressure Coefficient

Analysing the pressure drop fore to aft of the rotor, illustrated in Figure 16, a quasi-linear trend was apparent throughout the bearing range. Identical to the thrust and torque variations, the pressure difference at yaw bearings of $\gamma = 15^o, 23.2^o, 30^o$ were similar to that at aligned flows, with increased values at higher TSRs. The largest pressure difference along the curve was attained at the nominal bearing of $\gamma = 23.2^o$. A diminishment in pressure

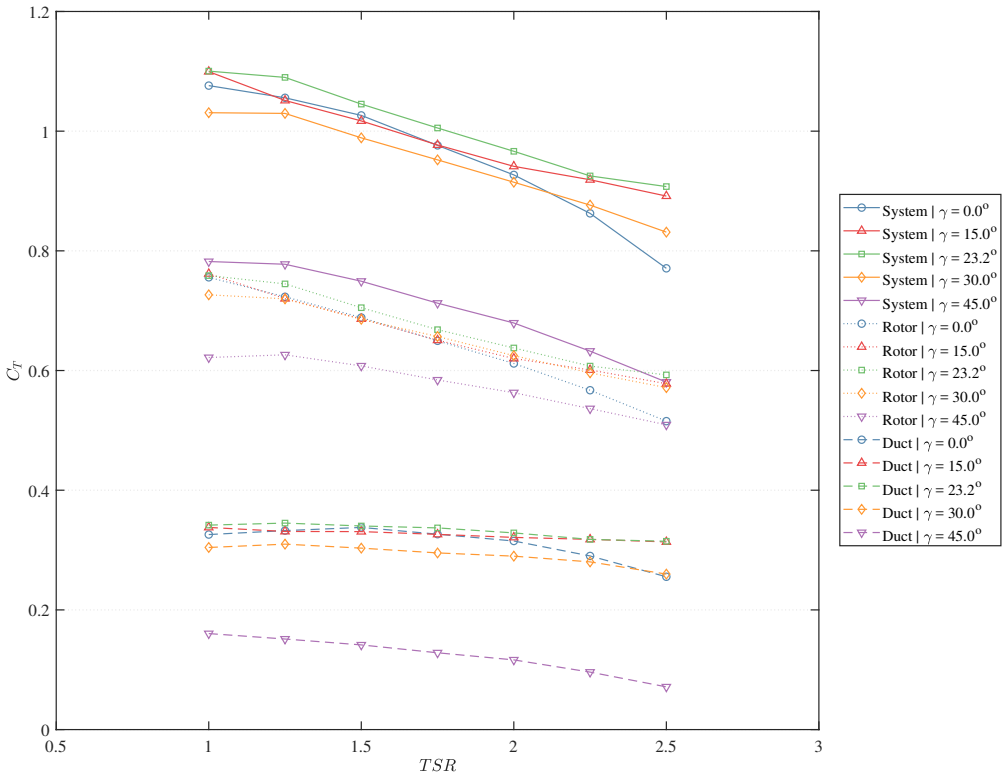

Figure 14: Evaluation of the mean ducted turbine thrust coefficient (C_T) at distinct flow bearings in relation to TSR

difference was attained at a yaw angle of $\gamma = 45^o$. The increase in static pressure difference at distinct bearings therefore elucidated the increased loading, and identified the causation in the enhanced torque and thrust.

Discretising the variation in static pressure difference by flow bearing, illustrated in Figure 17, the pressure difference values increased with a variation in bearing from aligned flow at $\gamma = 0^o$ to nominal bearing at $\gamma = 23.2^o$, attaining the highest values of pressure difference at the TSR range. The pressure difference then decreased at post-nominal angles ($\gamma > 23.2^o$).

In an effort to establish the variation in pressure difference, the pressure upstream and downstream of the rotor were analysed in segregation, illustrated in Figures 18 and 19 respectively. The pressure induced upstream of the rotor diminished in relation to an increase in yaw angle as the exposed frontal area of the duct inlet plane decreased. Ref. [33] analysed the variation in static pressure within the vacant duct, elaborating its decrease until the occurrence of flow separation. This response similarly transpired within the current analysis, yet flow separation without reattachment did not occur due to the presence of the rotor.

The downstream pressure, at the outlet of the duct, was more unique in response. When succumb to aligned flow, the static pressure increased in a polynomial manner in proportion to rotational velocity. Within yawed flow, the static pressure varied distinctively along the flow bearing range. At lower TSRs, the static pressure at all bearings increased with

20

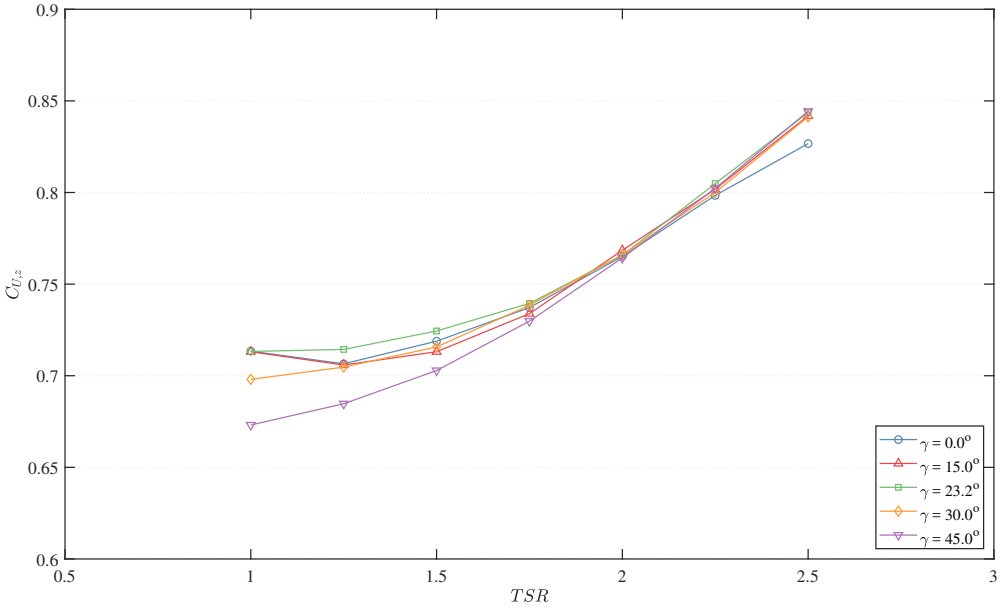

Figure 15: Evaluation of the mean axial velocity coefficient ($C_{U,z}$) at distinct flow bearings in relation to TSR

an enhancement in rotational velocity. Yet, towards higher TSRs, a diminishing trend in downstream pressure was acknowledged solely for non-aligned yaw bearings. The trend variation established the causation of the enhancement in static pressure drop.

Physically, within aligned flow, the wake exited the duct in a direction normal to the rotor plane, inducing back pressure at the duct outlet. Upon yawed flow, the free-stream interacted with the wake, shifting its orientation towards the flow bearing. As a result of the wake shift, the back pressure at the duct outlet diminished, thereby decreasing the static pressure downstream of the rotor.

5.3.3. Linear Momentum Thrust Coefficient

To verify the established results, linear momentum theory was implemented to determine the static pressure difference through the rotor in relation to the thrust upon the blades. Applying Equation 13, the disc thrust coefficient ($C_{T_{AD}}$) was compared to the blade-integrated thrust coefficient (C_T), as illustrated in Figure 20, attaining good comparison. The actuator disc outcomes were found to underestimate the result. Utilising the coefficient of determination (R^2), the relation between the two methodologies was 0.942, 0.915, 0.901, 0.862, and -0.770 for the bearings 0.0^o, 15.0^o, 23.2^o, 30.0^o, and 45.0^o, respectively. The coefficient of determination decreased proportional to the bearing angle, and negating at the highest bearing. This was due to the inapplicability of an area-averaged assumption at large yaw bearings as dynamic property inconsistencies, such as regions of flow separation, were brought about along the rotor area.

21

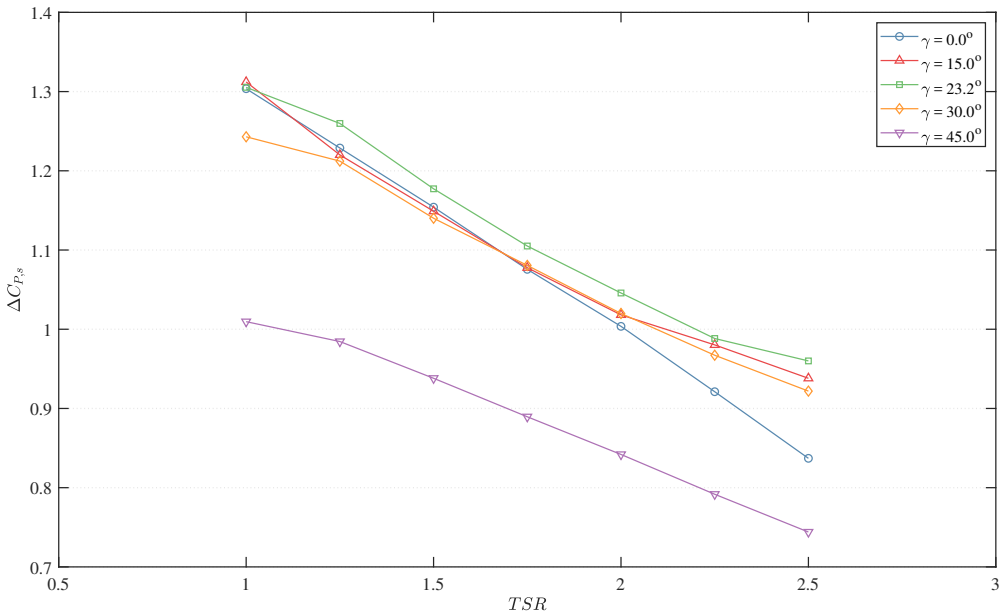

Figure 16: Evaluation of the mean static pressure difference coefficient ($\Delta C_{P,s}$) at distinct flow bearings in relation to TSR

5.4. Lateral Load Coefficient

The lateral force, acting perpendicular to the rotor axis, upon the turbine was established as a result of the free-stream bearing variation. Illustrated in Figure 21, the induced force enhanced proportionally to yaw bearing as the free-stream velocity vector component perpendicular to the turbine axis increased. Within aligned flows, minute lateral forces were generated upon the structure. At nominal bearing ($\gamma = 23.2^o$), a mean force coefficient of 0.411 was acknowledged. The resultant force was largely instigated upon the duct ($\approx 98\%$), with a minute degree of the resultant force acting upon the rotor.

5.5. Duct Static Pressure Coefficient

In analysis of a vacant duct [33], the variation in flow bearing shifted the angle-of-attack with the geometrical profile of the duct inlet. The stall limit was reached, inducing flow separation along the inner duct surface. To similarly acknowledge the effects of a yawed flow-stream upon the ducted turbine inlet, a static pressure distribution along the upstream section of the duct was established, depicted in Figure 22. The surfaces were discretised by their internal and external positions, in starboard and port directions.

Within aligned flows [34], pressure was sustained along the internal duct surface, whereas suction was dominant throughout the external duct surface. The pressure stagnation zone was present as a circular ring along the internal duct surface.

With an increase in yaw bearing, the pressure stagnation ring skewed. At $\gamma = 15^o, 23.2^o$, the stagnation ring was sustained along the internal duct surface. At starboard, the stagnation point shifted into the duct, closer to the rotor. At port, the stagnation point shifted away from the rotor, with that at $\gamma = 23.2^o$ present at the inlet leading edge.

22

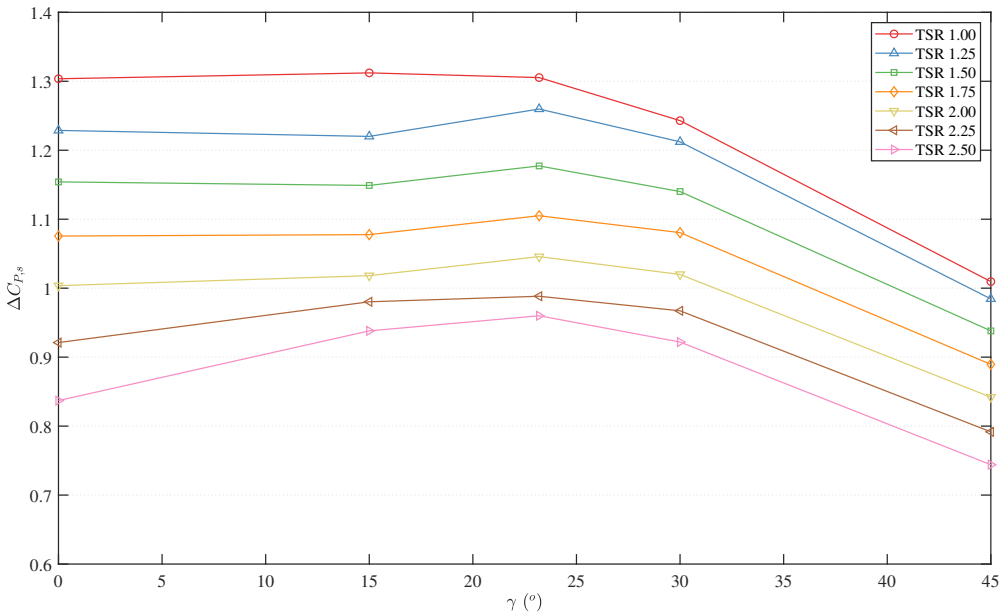

Figure 17: Evaluation of the mean static pressure difference coefficient ($\Delta C_{P,s}$) at distinct TSRs in relation to flow bearing (γ)

At $\gamma = 30^o, 45^o$, the stagnation ring overlapped upon the internal and external duct surfaces. The stagnation point at starboard was retained upon the internal duct surface, shifting further into the duct, whereas the stagnation point at port was present upon the external duct surface. Figure 23 puts forward a qualitative illustration of the upstream stream-tube boundaries, acknowledging the points of stagnation.

Along the internal surfaces, pressure was predominantly sustained at starboard. At port, a diminishment in pressure was acknowledged relative to yaw angle, with suction being dominant at $\gamma = 30^o, 45^o$. Along the external surfaces, pressure was sustained at port, whereas suction was dominant at starboard.

5.6. Wake Profiles

In visualising the velocity flow contours of the domain, the wake varied in orientation to the flow bearing, as illustrated in Figure 24. As a result of the shift, vorticial flow was generated along the duct structure, portraying blunt body properties. Distinctively focusing upon the port side of the turbine, the generation of flow separation in relation to yaw bearing is illustrated in Figure 25. At $\gamma = 0^o$, flow was consistent within the duct. At $\gamma = 23.2^o$, slight flow separation occurred, which recovered upstream of the rotor. At $\gamma = 45^o$, significant flow separation was present upstream of the rotor. At the flow bearing, the separated flow did not recover, resulting in a re-circulation zone to be developed immediately upstream of the rotor, establishing a region of low pressure interacting with the blades at port. The production of a re-circulation zone at a distinct angle-of-attack had been acknowledged by Borg et al. [33] due to the low-pressure zone induced within the duct, occurring as the yaw bearing approached and exceeded the stall angle of the duct inlet,

23

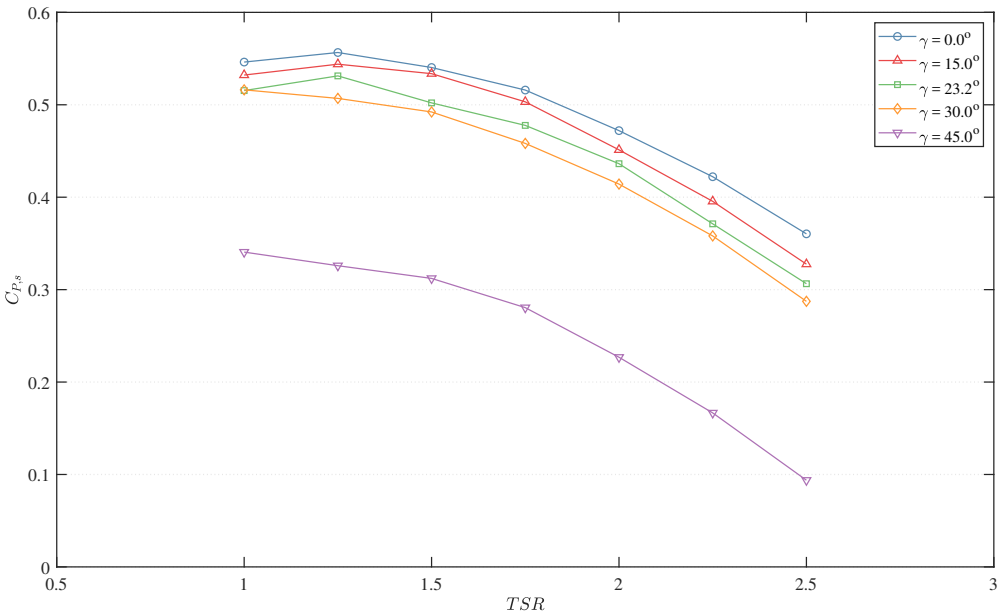

Figure 18: Evaluation of the mean static pressure coefficient ($C_{P,s}$) upstream at distinct flow bearings in relation to TSR

resulting in the production of flow separation. The flow structure induced the dip in torque at an azimuth angle of 90^o.

6. Conclusion

This study put forward an investigation into the hydrodynamic performance of a ducted, high-solidity tidal turbine in yawed flow conditions utilising blade-resolved, unsteady computational fluid dynamics, coupled with the τ-ω Reynolds-Stress Model turbulence model. The research strived to overcome the limitations of prior analyses by acknowledging the explicit physicality of the rotor blades.

Through blade-integrated results, the power coefficient was found to increase at higher rotational velocities within the 15^o - 30^o yaw angular range. At these conditions, the maximum power coefficient was found to reach a value of 0.35 at a bearing of 23.2^o. In recognition, the induced thrust was analysed, noting an increase in axial loading within the yaw range at higher tip-speed ratios.

Acknowledging the parametric variation, linear momentum theory was utilised in an effort to verify the portrayed characteristics. Area-averaged outcomes of axial velocity and static pressure were extracted from implemented numerical planes created fore and aft of the rotor within the CFD model. It was established that, due to the presence of the duct, the axial velocity was sustained through the rotor. Further to this, the pressure difference across the rotor augmented within the yaw bearing range, peaking at $\gamma = 23.2^o$. The increase was due to the diminishment of static pressure at the outlet of the duct at higher TSRs. Post-nominal bearings portrayed a decrease in pressure difference due to flow separation induced upstream of the rotor. Power augmentation was hence restricted by the stall limit

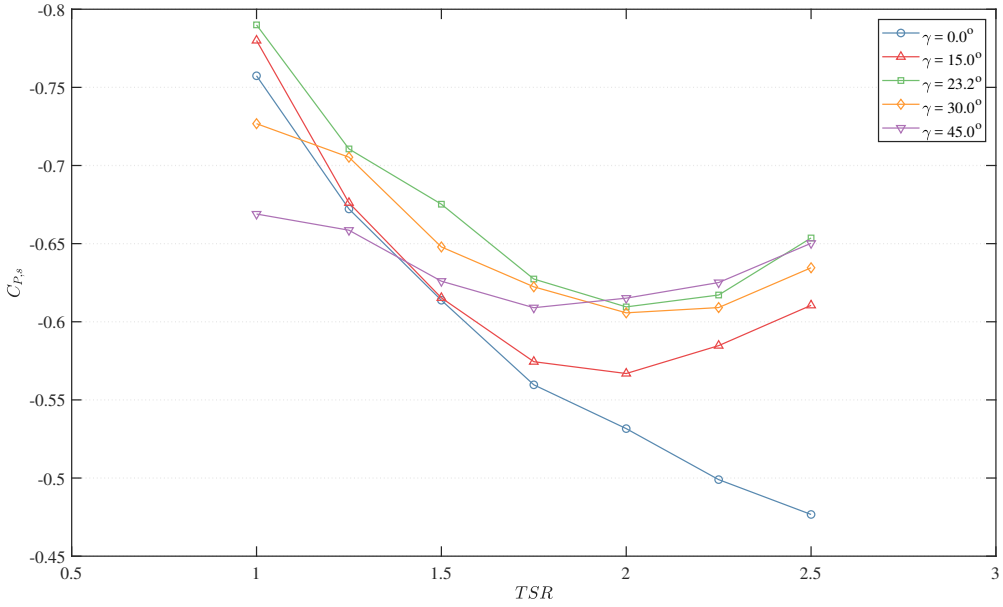

Figure 19: Evaluation of the mean static pressure coefficient ($C_{P,s}$) downstream at distinct flow bearings in relation to TSR

of the shroud inlet profile. Albeit the advantageous enhancement and sustainment of the turbine power coefficient at distinct flow bearings, Borg et al. [35] acknowledged that the rotor blades may be succumb to substantial vibrational effects, bringing about an increased possibility of failure by fatigue throughout operation.

It was concluded that the duct installation sustained axial velocity along the bearing range, together with inducing a diminishment in pressure downstream of the rotor, resulting in an augmented pressure drop. The rotor thrust, in conjunction with torque and power, was hence enhanced, ensuing in the performance improvement of the ducted turbine.

Acknowledgements

The research work disclosed in this publication is partially financed by the European Union – European Social Fund (ESF) – Operational Programme II – Cohesion Policy 2014-2020.

Results were obtained using ARCHIE-WeSt High Performance Computer (www.archie-west.ac.uk).

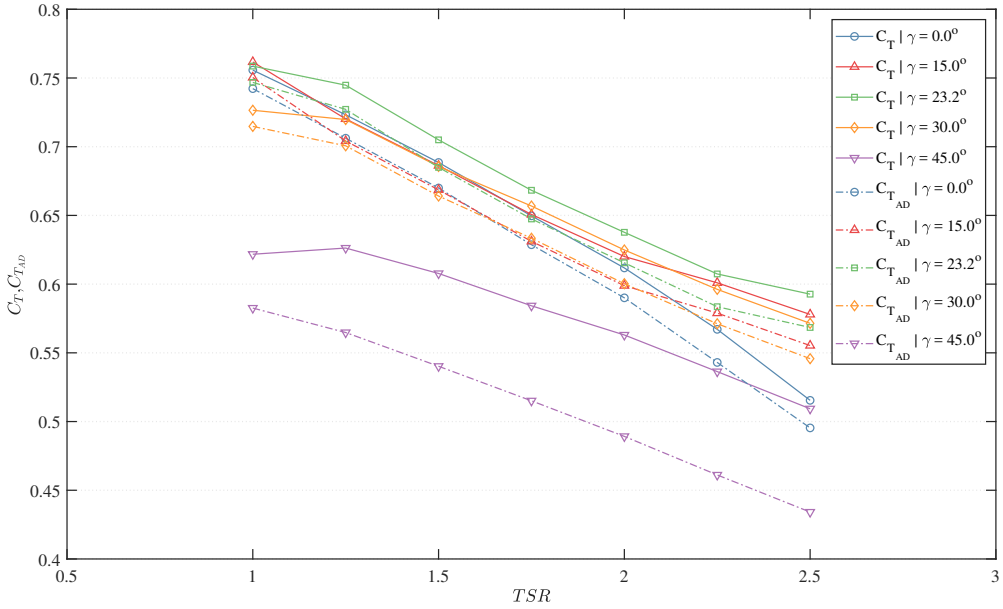

Figure 20: Evaluation of the mean blade thrust coefficient (C_T) with the mean linear momentum thrust ($C_{T_{AD}}$) at distinct flow bearings in relation to TSR

References

[1] F. O Rourke, F. Boyle, and A. Reynolds, "Tidal energy update 2009," *Applied Energy*, vol. 87, no. 2, pp. 398–409, 2010.

[2] A. Kogan and A. Seginer, "T.A.E. Rep. No. 32A: Final report on shroud design," tech. rep., Department of Aeronautical Engineering, Technion – Israel Institute of Technology, Haifa, Israel, 1963.

[3] K. Foreman, B. Gilbert, and R. Oman, "Diffuser augmentation of wind turbines," *Solar Energy*, vol. 20, no. 4, pp. 305 – 311, 1978.

[4] O. Igra, "Research and development for shrouded wind turbines," *Energy Conversion and Management*, vol. 21, no. 1, pp. 13–48, 1981.

[5] D. G. Phillips, *An investigation on diffuser augmented wind turbine design*. PhD thesis, The University of Auckland, 2003.

[6] C. Belloni, R. Willden, and G. Houlsby, "An investigation of ducted and open-centre tidal turbines employing CFD-embedded BEM," *Renewable Energy*, vol. 108, pp. 622–634, 8 2017.

[7] P. Liu and N. Bose, "Prototyping a series of bi-directional horizontal axis tidal turbines for optimum energy conversion," *Applied Energy*, vol. 99, pp. 50 – 66, 2012.

[8] N. W. Cresswell, G. Ingram, and R. Dominy, "The impact of diffuser augmentation on a tidal stream turbine," *Ocean Engineering*, vol. 108, pp. 155–163, 10 2015.

[9] G. M. Lilley and W. J. Rainbird, "A preliminary report on the design and performance of ducted windmills," Tech. Rep. 102, College of Aeronautics, Cranfield, Bedfordshire, United Kingdom, 04 1956.

[10] G. Riegler, "Principles of energy extraction from a free stream by means of wind turbines," *Wind Engineering*, vol. 7, no. 2, pp. 115–126, 1977.

[11] Bloomberg L.P., "OpenHydro Group Limited: Private Company Information - Bloomberg," 2018.

[12] OpenHydro Group Ltd., "Projects," 2016.

[13] Y. Ohya, T. Karasudani, A. Sakurai, K. Abe, and M. Inoue, "Development of a shrouded wind turbine with a flanged diffuser," *Journal of Wind Engineering and Industrial Aerodynamics*, vol. 96, pp. 524–539, 6 2008.

[14] O. Igra, "Compact shrouds for wind turbines," *Energy Conversion*, vol. 16, pp. 149–157, 1 1977.

[15] Y. Ohya, T. Karasudani, A. Sakurai, K.-i. Abe, and M. Inoue, "Development of a shrouded wind

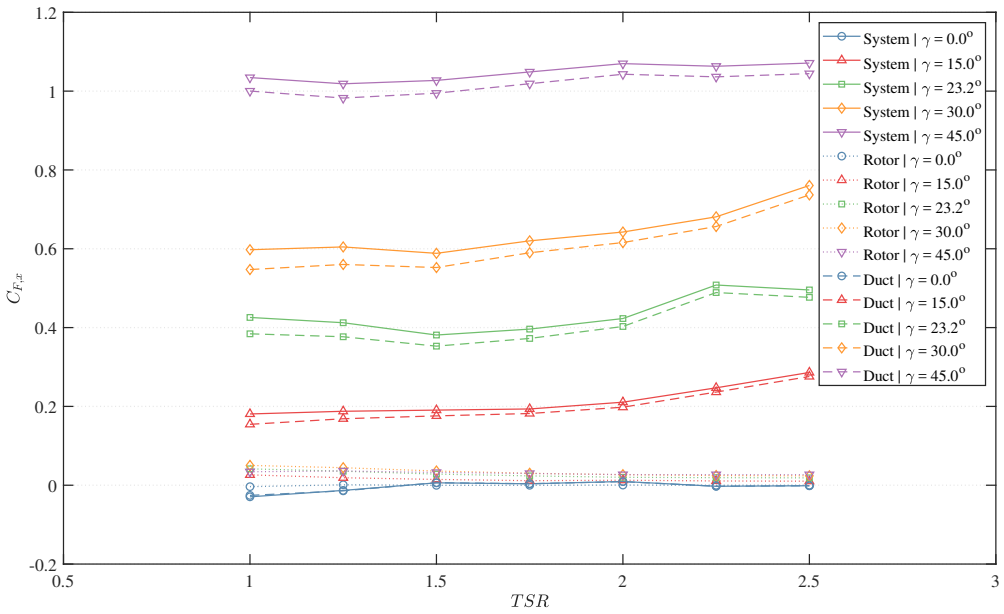

Figure 21: Evaluation of the mean lateral load coefficient ($C_{F,x}$) at distinct flow bearings in relation to TSR

turbine with a flanged diffuser," *Journal of Wind Engineering and Industrial Aerodynamics*, vol. 96, pp. 524–539, 5 2008.

[16] B. Gilbert, R. Oman, and K. Foreman, "Fluid Dynamics of Diffuser-Augmented Wind Turbines," *Journal of Energy*, vol. 2, pp. 368–374, 11 1978.

[17] O. Igra, "Design and Performance of a Turbine Suitable for an Aerogenerator," *Energy Conversion*, vol. 15, pp. 143–151, 1 1976.

[18] O. Igra, "The shrouded aerogenerator," *Energy*, vol. 2, pp. 429–439, 2 1977.

[19] B. Kosasih and A. Tondelli, "Experimental Study of Shrouded Micro-Wind Turbine," *Procedia Engineering*, vol. 49, pp. 92–98, 11 2012.

[20] I. Grant, P. Parkin, and X. Wang, "Optical vortex tracking studies of a horizontal axis wind turbine in yaw using laser-sheet, flow visualisation," *Experiments in Fluids*, vol. 23, pp. 513–519, 1997.

[21] R. Bontempo and M. Manna, "Performance analysis of open and ducted wind turbines," *Applied Energy*, vol. 136, pp. 405–416, 2014.

[22] R. Bontempo and M. Manna, "A ring-vortex actuator disk method for wind turbines including hub effects," *Energy Conversion and Management*, vol. 195, pp. 672 – 681, 2019.

[23] R. Bontempo and M. Manna, "On the potential of the ideal diffuser augmented wind turbine: an investigation by means of a momentum theory approach and of a free-wake ring-vortex actuator disk model," *Energy Conversion and Management*, vol. 213, p. 112794, 2020.

[24] D. G. Phillips, P. J. Richards, G. D. Mallinson, and R. G. J. Flay, "Computational Modelling of Diffuser Designs for a Diffuser Augmented Wind Turbine," in *Australasian Fluid Mechanics Conference*, 13th, (Melbourne, Australia), pp. 207–210, Australasian Fluid Mechanics Society (AFMS), December 1998.

[25] V. Dighe, D. Suri, F. Avallone, and G. van Bussel, "Ducted wind turbines in yawed flow: A numerical study," *Wind Energy Science Discussions*, vol. 2019, pp. 1–13, 2019.

[26] D. L. Gaden and E. L. Bibeau, "A numerical investigation into the effect of diffusers on the performance of hydro kinetic turbines using a validated momentum source turbine model," *Renewable Energy*, vol. 35, no. 6, pp. 1152 – 1158, 2010.

[27] M. O. L. Hansen, N. N. Sørensen, and R. G. J. Flay, "Effect of Placing a Diffuser around a Wind Turbine," *Wind Energy*, vol. 3, pp. 207–213, 10 2000.

[28] C. S. Belloni, R. H. Willden, and G. T. Houlsby, "A Numerical Analysis of Bidirectional Ducted Tidal

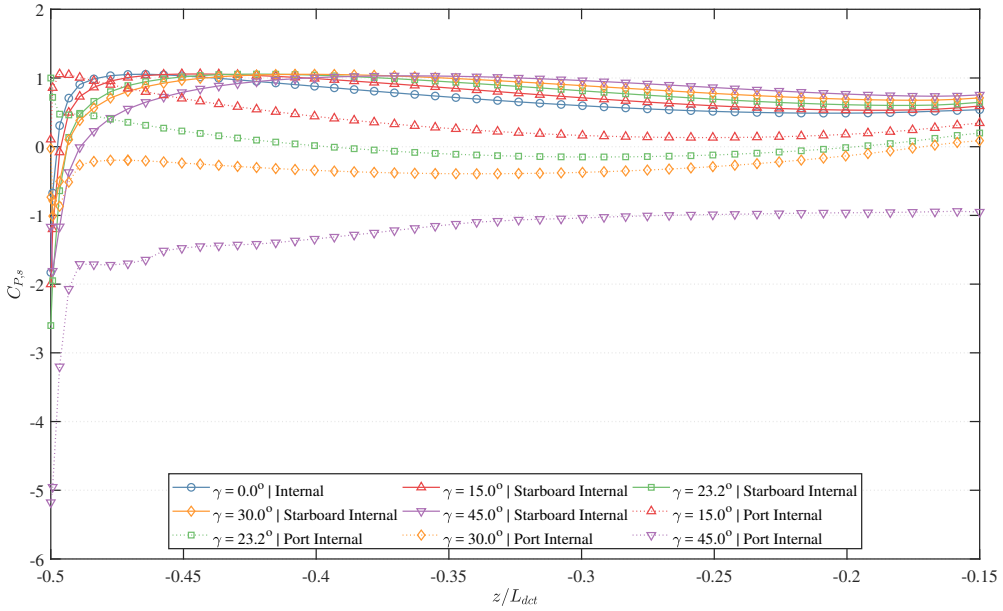

(a) Pressure coefficient along the internal duct surfaces

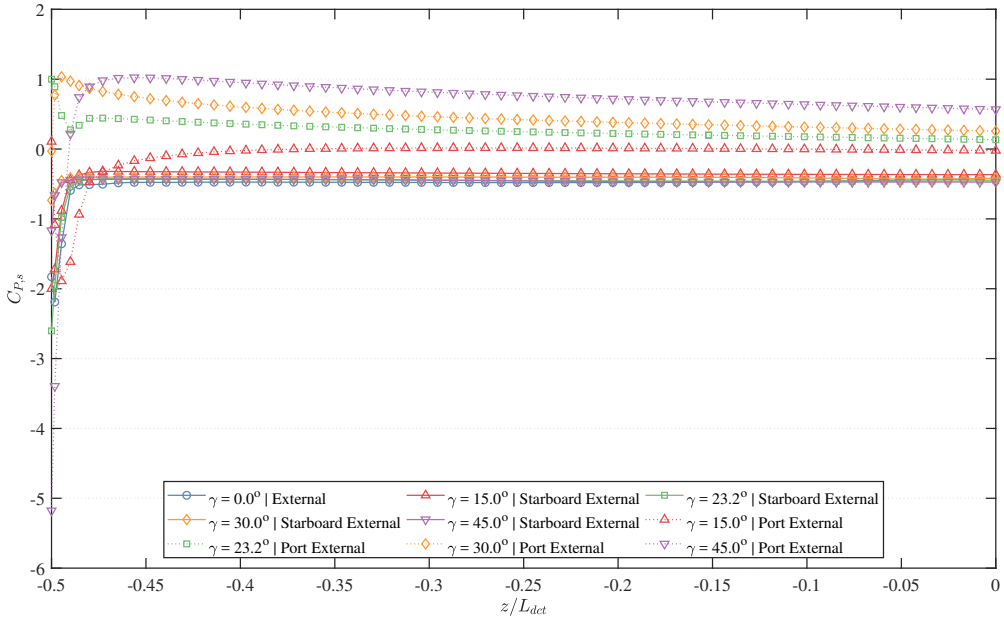

(b) Pressure coefficient along the external duct surfaces

Figure 22: Evaluations of static pressure coefficient ($C_{P,s}$) distribution along the duct inlet surfaces

Turbines in Yawed Flow," *Marine Technology Society Journal*, vol. 47, pp. 23–35, 7 2013.

[29] R. Luquet, D. Bellevre, D. Fréchou, P. Perdon, and P. Guinard, "Design and model testing of an optimized ducted marine current turbine," *International Journal of Marine Energy*, vol. 2, pp. 61–80, 6 2013.

[30] A. C. Aranake, V. K. Lakshminarayan, and K. Duraisamy, "Computational analysis of shrouded wind turbine configurations using a 3-dimensional rans solver," *Renewable Energy*, vol. 75, pp. 818–832, 2015.

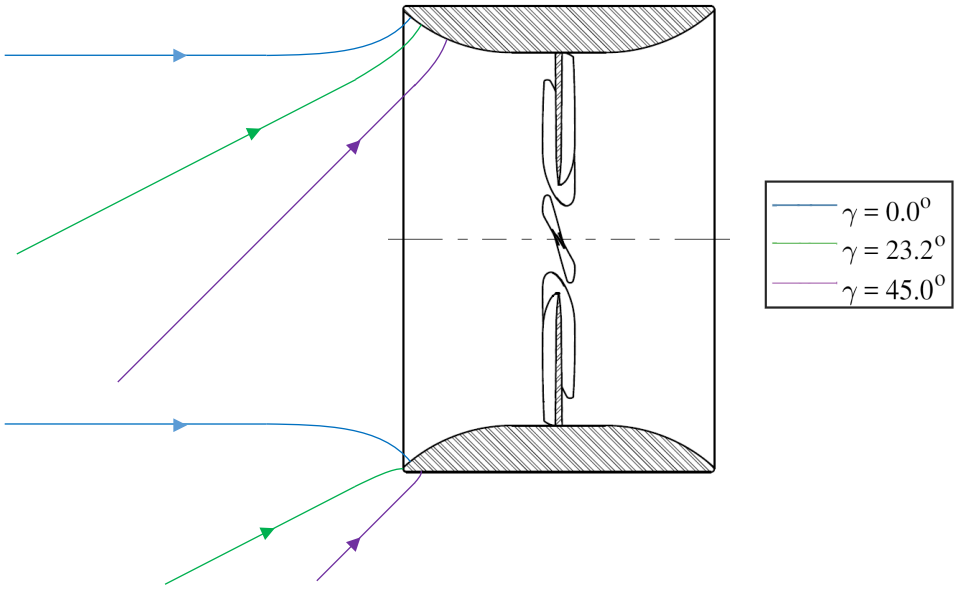

Figure 23: Illustrative representation of the upstream stream-tube boundaries at the duct inlet

[31] B. Hadya and J. Pailla, "Performance analysis of an omnidirectional intake duct wind turbine using cfd," *International Journal of Latest Engineering and Management Research (IJLEMR)*, vol. 02, pp. 01–10, September 2017.

[32] A. Saleem and M.-H. Kim, "Effect of rotor tip clearance on the aerodynamic performance of an aerofoil-based ducted wind turbine," *Energy Conversion and Management*, vol. 201, p. 112186, 2019.

[33] M. G. Borg, Q. Xiao, S. Allsop, A. Incecik, and C. Peyrard, "A numerical swallowing-capacity analysis of a vacant, cylindrical, bi-directional tidal turbine duct in aligned & yawed flow conditions," *Journal of Marine Science and Engineering*, vol. 9, no. 2, 2021.

[34] M. G. Borg, Q. Xiao, S. Allsop, A. Incecik, and C. Peyrard, "A numerical performance analysis of a ducted, high-solidity tidal turbine," *Renewable Energy*, vol. 159, pp. 663 – 682, 2020.

[35] M. G. Borg, Q. Xiao, S. Allsop, A. Incecik, and C. Peyrard, "A numerical structural analysis of ducted, high-solidity, fibre-composite tidal turbine rotor configurations in real flow conditions," *Ocean Engineering*, vol. 233, p. 109087, 2021.

[36] A. Betz, "Windmills in the light of modern research," tech. rep., National Advisory Committee for Aeronautics, Washington, DC, 8 1928.

[37] S. Allsop, C. Peyrard, P. R. Thies, E. Boulougouris, and G. P. Harrison, "Hydrodynamic analysis of a ducted, open centre tidal stream turbine using blade element momentum theory," *Ocean Engineering*, vol. 141, pp. 531–542, 9 2017.

[38] C.-T. Pham and V. A. Martin, "Tidal current turbine demonstration farm in paimpol-brehat (brittany): tidal characterisation and energy yield evaluation with telemac," in *Proceedings of the 8th European Wave and Tidal Energy Conference, Uppsala, Sweden*, vol. 710, 2009.

[39] C. Pham and K. Pinte, "Paimpol brehat tidal turbine demonstration farm (brittany): optimisation of the layout, wake effects and energy yield evaluation using telemac," in *3rd International Conference on Ocean Energy*, 2010.

[40] P. Mycek, B. Gaurier, G. Germain, G. Pinon, and E. Rivoalen, "Renewable Energy Experimental study of the turbulence intensity effects on marine current turbines behaviour. Part I: One single turbine," *Renewable Energy*, vol. 66, pp. 729–746, 2014.

[41] S. C. Allsop, *Hydrodynamic Modelling for Structural Analysis of Tidal Stream Turbine Blades*. PhD thesis, University of Edinburgh, 6 2018.

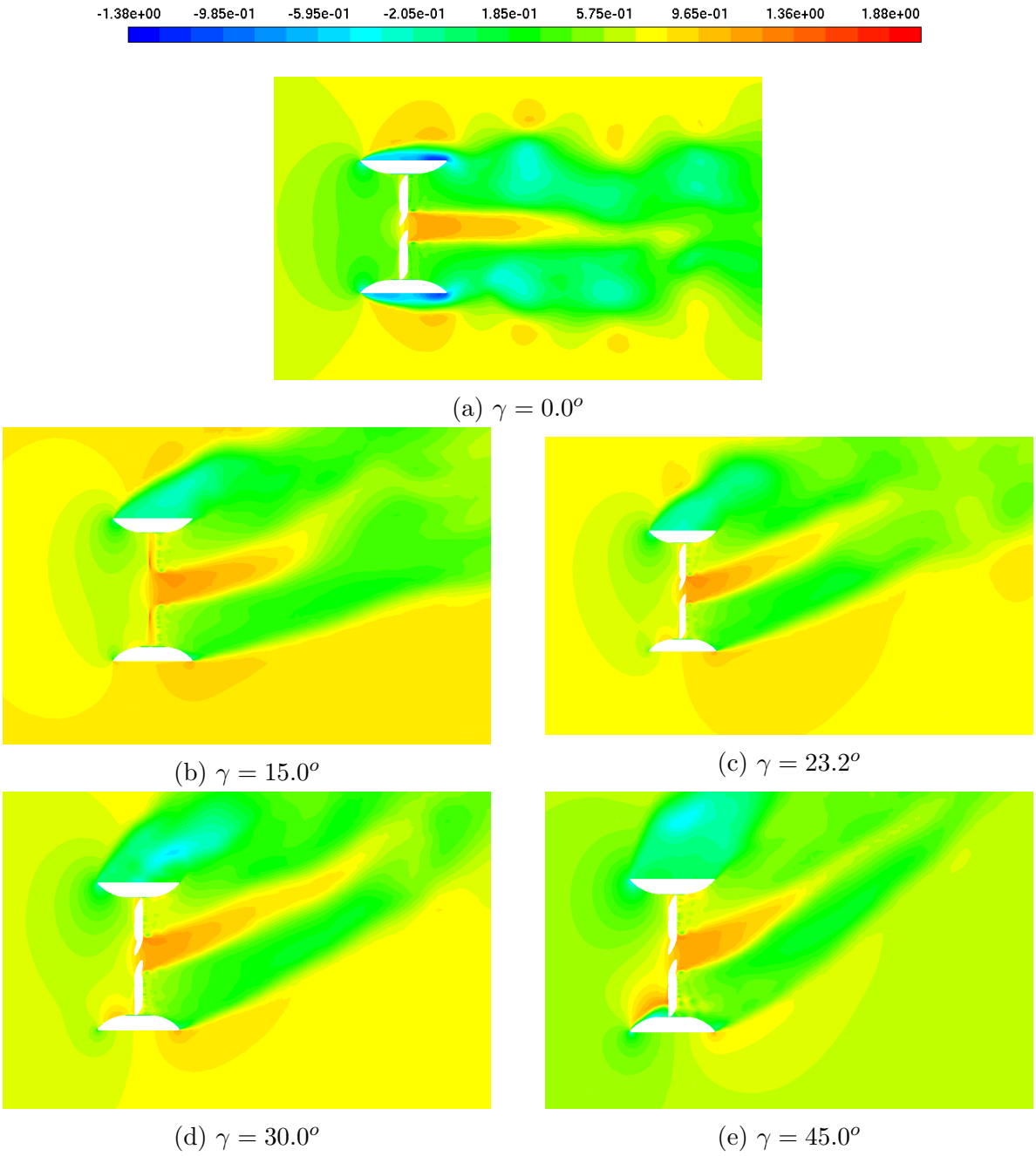

(a) $\gamma = 0.0^o$

(b) $\gamma = 15.0^o$

(c) $\gamma = 23.2^o$

(d) $\gamma = 30.0^o$

(e) $\gamma = 45.0^o$

Figure 24: Illustrative top-view representation of the axial velocity coefficient ($C_{U,z}$) within the turbine domain at distinct flow bearings

[42] S. P. Neill, J. R. Jordan, and S. J. Couch, "Impact of tidal energy converter (TEC) arrays on the dynamics of headland sand banks," *Renewable Energy*, vol. 37, pp. 387–397, 1 2012.

[43] A. Bahaj and L. Myers, "Analytical estimates of the energy yield potential from the Alderney Race (Channel Islands) using marine current energy converters," *Renewable Energy*, vol. 29, pp. 1931–1945, 10 2004.

[44] A. Mason-Jones, D. M. O'Doherty, C. E. Morris, T. O'Doherty, C. B. Byrne, P. W. Prickett, R. I.

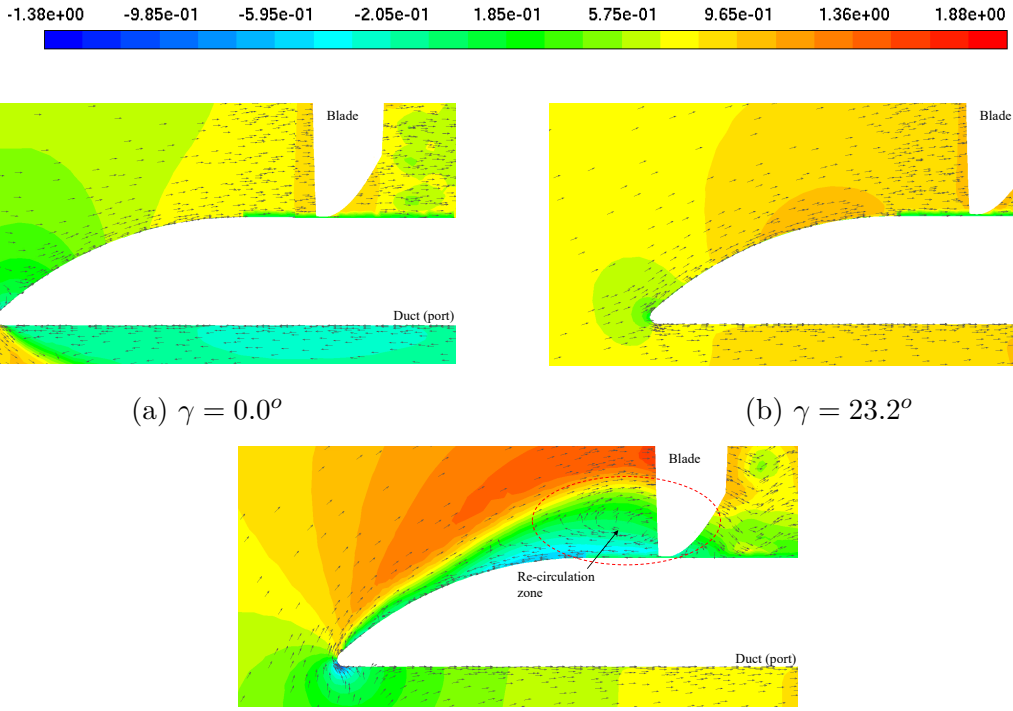

(a) $\gamma = 0.0^o$ (b) $\gamma = 23.2^o$

(c) $\gamma = 45.0^o$

Figure 25: Illustrative top-view representation of the axial velocity coefficient ($C_{U,z}$) at port-side duct, focusing on the induced re-circulation zone region

Grosvenor, I. Owen, S. Tedds, and R. J. Poole, "Non-Dimensional Scaling of Tidal Stream Turbines," *Energy*, vol. 44, pp. 820–829, 2012.

[45] D. C. Wilcox, *Turbulence Modeling for CFD, Third Edition*. San Diego: DCW Industries, Inc, third ed., 2006.

[46] R. C. of the 25th ITTC, "Uncertainty analysis in cfd verification and validation methodology and procedures," tech. rep., 2008.

Appendix A. Axial Velocity

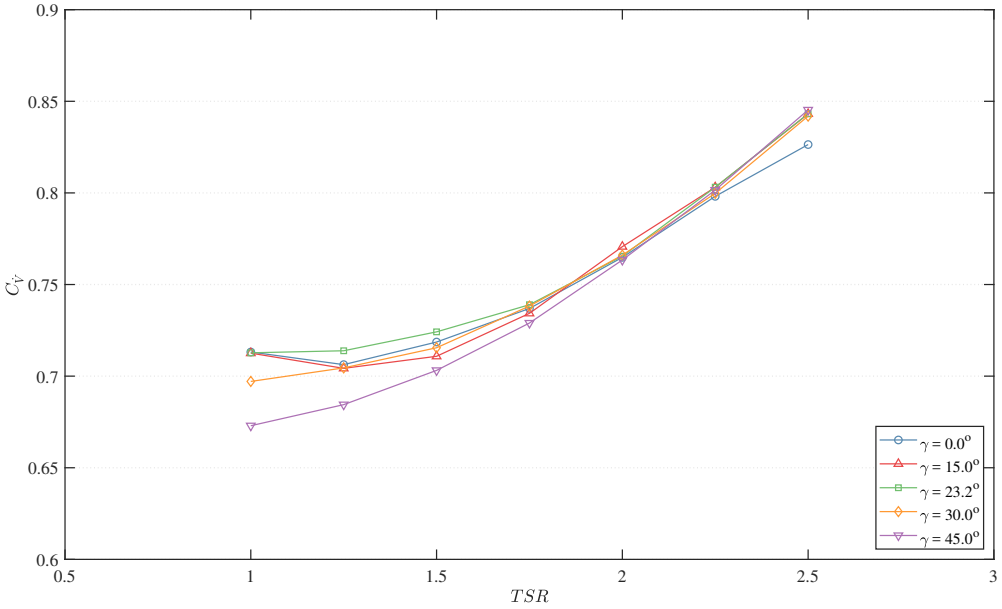

Figure A.26: Evaluation of the mean volumetric flow-rate coefficient ($C_{\dot{V}}$) at distinct flow bearings in relation to TSR

32

Appendix B. Torque & Thrust Coefficient Standard Deviation

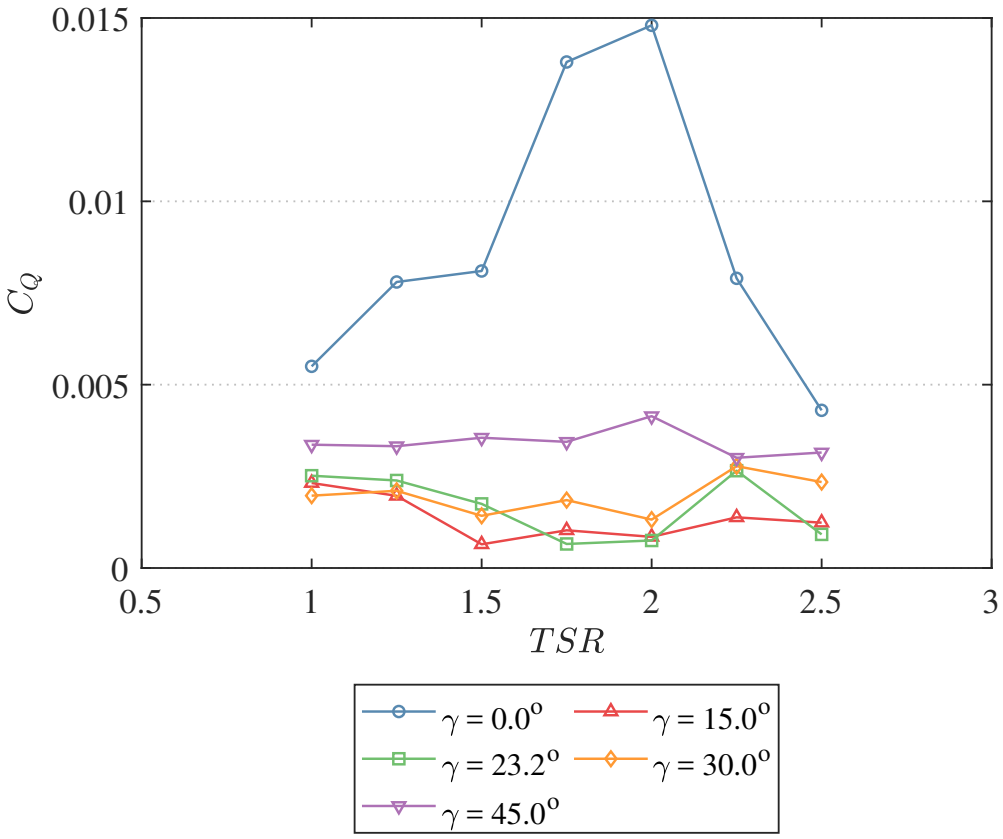

Figure B.27: Evaluation of the torque coefficient (C_Q) standard deviation at distinct flow bearings in relation to TSR

33

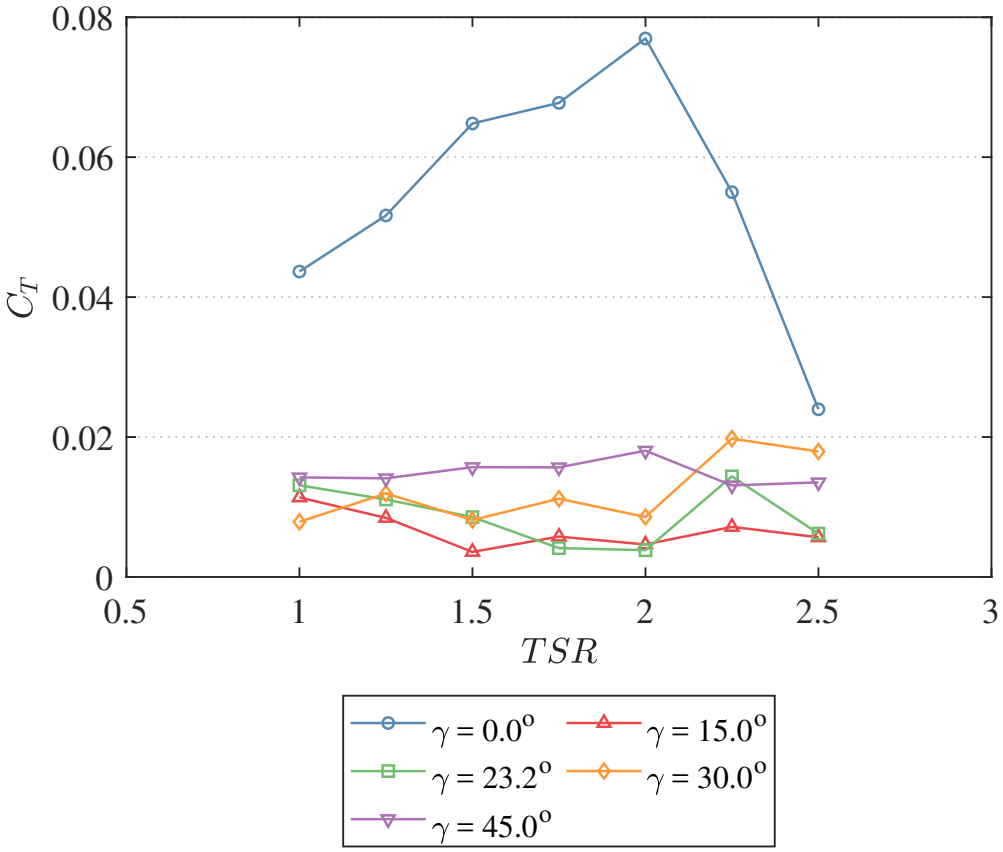

Figure B.28: Evaluation of the thrust coefficient (C_T) standard deviation at distinct flow bearings in relation to TSR

34